

Non-Gaussian noise spectroscopy with a superconducting qubit sensor

Youngkyu Sung^{1,2}, Félix Beaudoin³, Leigh M. Norris³, Fei Yan¹, David K. Kim⁴, Jack Y. Qiu^{1,2}, Uwe von Lüpke¹, Jonilyn L. Yoder⁴, Terry P. Orlando^{1,2}, Simon Gustavsson¹, Lorenza Viola^{*3}, and William D. Oliver^{†1,2,4,5}

¹Research Laboratory of Electronics, Massachusetts Institute of Technology, Cambridge, MA 02139, USA

²Department of Electrical Engineering and Computer Science, Massachusetts Institute of Technology, Cambridge, MA 02139, USA

³Department of Physics and Astronomy, Dartmouth College, Hanover, NH 03755, USA

⁴MIT Lincoln Laboratory, 244 Wood Street, Lexington, MA 02421, USA

⁵Department of Physics, Massachusetts Institute of Technology, Cambridge, MA 02139, USA

October 2, 2019

Accurate characterization of the noise influencing a quantum system of interest has far-reaching implications across quantum science, ranging from microscopic modeling of decoherence dynamics to noise-optimized quantum control. While the assumption that noise obeys Gaussian statistics is commonly employed, noise is generically non-Gaussian in nature. In particular, the Gaussian approximation breaks down whenever a qubit is strongly coupled to discrete noise sources or has a non-linear response to the environmental degrees of freedom. Thus, in order to both scrutinize the applicability of the Gaussian assumption and capture distinctive non-Gaussian signatures, a tool for characterizing non-Gaussian noise is essential. Here, we experimentally validate a quantum control protocol which, in addition to the spectrum, reconstructs the leading higher-order spectrum of engineered non-Gaussian dephasing noise using a superconducting qubit as a sensor. This first experimental demonstration of non-Gaussian noise spectroscopy represents a major step toward demonstrating a complete spectral estimation toolbox for quantum devices.

Introduction

For any dynamical system that evolves in the presence of unwanted disturbances, precise knowledge of the noise spectral features is fundamental for quantitative understanding and prediction of the dynamics under realistic conditions. As a result, spectral estimation techniques have a long tradition and play a central role in classical statistical signal processing [1]. For quantum systems, the importance of precisely characterizing noise effects is further heightened by the challenge of harnessing the practical potential that quantum science and technology applications promise. Such detailed knowledge is key to develop noise-optimized strategies for enhancing quantum coherence and boosting control fidelity in near-term intermediate-scale quantum information processors [2], as well as for over-

coming noise effects in quantum metrology [3, 4]. Ultimately, probing the extent and decay of noise correlations will prove crucial in determining the viability of large-scale fault-tolerant quantum computation [5].

Thanks to their exquisite sensitivity to the surrounding environment, qubits driven by external control fields are naturally suited as “spectrometers,” or sensors, of their own noise [6, 7]. Quantum noise spectroscopy (QNS) leverages the fact that open-loop control modulation is akin to shaping the filter function that determines the sensor’s response in frequency space [8–12] and, in its simplest form, aims to characterize the spectral properties of environmental noise as sensed by a single qubit sensor. By now, QNS protocols employing both pulsed and continuous control modalities have been explored, and experimental implementations have been reported across a wide variety of qubit platforms – including NMR [13], superconducting quantum circuits [14–17], semiconductor quantum dots [18–21], diamond nitrogen vacancy centers [22, 23], and trapped ions [24]. Notably, knowledge of the underlying noise spectrum has already enabled unprecedented coherence times to be achieved via tailored error suppression [25].

While the above advances clearly point to the growing significance of spectral estimation in the quantum setting, they all rely on the assumption that the target noise process is Gaussian – that is, one- and two-point correlation functions suffice to fully specify the noise statistical properties. However, the Gaussian assumption need not be justified *a priori* and it should rather be validated (or falsified) by the QNS protocol itself. A number of realistic scenarios motivate the consideration of non-Gaussian noise regimes. Statistical processes that are responsible for electronic current fluctuations in mesoscopic devices or the $1/f$ noise ubiquitously encountered in solid-state quantum devices are not Gaussian in general [26]. In superconducting circuits, previous studies have shown that a few two-level defects within Josephson tunnel junctions can interact strongly with the qubit [27–31], the resulting decoherence dynamics showing marked deviations from Gaussian behavior under both free evolution and dynamical decoupling protocols [7, 32, 33]. More generally, non-Gaussian noise statistics may be expected to arise whenever a qubit is operated outside a linear-response regime, either due to strong coupling to a discrete environment [34] or to a non-linear energy dispersion relationship. The latter

*lorenza.viola@dartmouth.edu

†william.oliver@mit.edu

feature, which has long been appreciated to influence dephasing behavior at optimal points [35], is common to all state-of-the-art superconducting qubit archetypes [36–39]. Thus, statistical correlations higher than second order and their corresponding multi-dimensional Fourier transforms must be taken into account for complete characterization. From a signal processing standpoint, this translates into the task of higher-order spectral estimation [40].

In this work, we experimentally demonstrate non-Gaussian QNS by building on the estimation procedure proposed by Norris *et al.* [41]. While we employ a flux-tunable superconducting qubit as a sensor, our methodology is portable to other physical testbeds in which classical dephasing noise is the dominant decoherence mechanism. We show how non-Gaussianity distinctively modifies the phase evolution of the sensor’s coherence, resulting in an observable signature to which the spectrum (or power spectral density, PSD) is completely insensitive and which is instead encoded in the leading higher-order spectrum, the bispectrum. Unlike the original proposal [41], the QNS protocol we introduce here makes use of a statistically-motivated maximum likelihood approach. This renders the estimation less susceptible to numerical instability, while allowing measurement errors to be incorporated and both the PSD and the bispectrum to be inferred using a single measurement setup. In order to obtain a clean benchmark for our spectral estimation procedure, we engineer a non-Gaussian noise model by injecting Gaussian flux at the sensor’s degeneracy point, resulting in non-Gaussian frequency noise. The noise implementation is validated by verifying the observed power dependence of the leading cumulants against the expected one. Both the reconstructed PSD and the bispectrum are found to be in quantitative agreement with theoretical predictions within error bars.

Results

Non-Gaussian dephasing noise

Before introducing our experimental test bed, we present the general setting to which our analysis is relevant: a qubit sensor evolving under the combined action of non-Gaussian classical dephasing noise and suitably designed sequences of control pulses. By working in an interaction frame with respect to the internal qubit Hamiltonian and the applied control, and letting $\hbar = 1$, the controlled open-system Hamiltonian may be written as $H(t) = y_p(t)B(t)\sigma_z/2$, where $B(t)$ is a stochastic process describing dephasing noise relative to the qubit’s eigenbasis defined by the Pauli operator σ_z . The control switching function $y_p(t)$ accounts for a sequence p of instantaneous π rotations about the x or y axis, starting from initial value $y_p(0) = +1$ and toggling between ± 1 with every application of a pulse. Under such a pure-dephasing Hamiltonian, the qubit coherence is quantified by the time-dependent expectation value $\langle \sigma_+(t) \rangle \equiv e^{-\chi(t)+i\phi(t)} \langle \sigma_+(0) \rangle$, where the influence of the noise is captured by the decay and phase parameters $\chi(t)$ and $\phi(t)$. These parameters may be formally expanded in terms of noise cumulants, $C^{(k)}(t_1, \dots, t_k)$, $k \in \{1, 2, \dots, \infty\}$, with $\chi(t)$ taking contribution only from even cumulants and $\phi(t)$ only from odd cumulants [41]. Physically, the k -th order cumulant is determined by the multi-time correlation functions $\mathbb{E}[B(t_1), \dots, B(t_j)]$, with $j \leq k$, where $\mathbb{E}[\cdot]$ denotes the ensemble average over noise realizations.

Since the statistical properties of Gaussian noise are entirely determined by one- and two-point correlation functions, cumu-

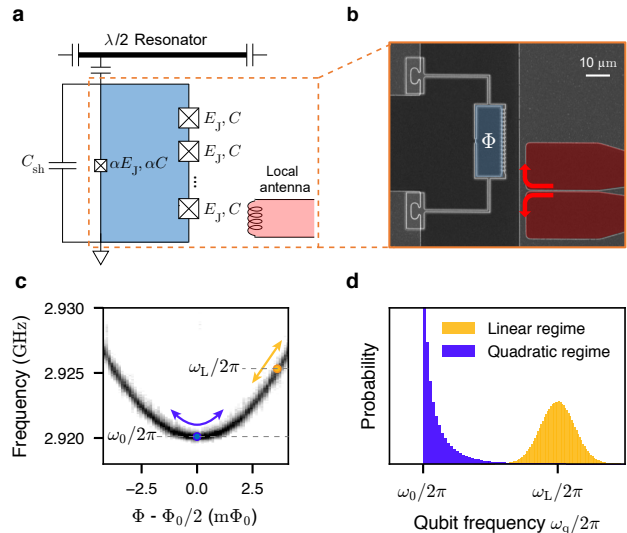


Figure 1. Experimental setup and non-Gaussian dephasing noise in a superconducting qubit. **a**, Schematic of the circuit QED system. An engineered flux qubit comprises a superconducting loop (blue) interrupted by one small-area and 8 large-area Josephson junctions (crosses) and is inductively coupled to a local antenna (red). The qubit junctions have internal capacitance, C and αC , and are externally shunted by capacitance C_{sh} . See Supplementary Note 1. **b**, SEM image of the device. The flux threading the qubit loop Φ is modulated by applying a current through the local antenna. **c**, Frequency spectroscopy of the qubit’s $|0\rangle \rightarrow |1\rangle$ transition. At (away from) the degeneracy point $\Phi = \Phi_0/2$, the qubit frequency ω_q has a quadratic (linear) dependence on the external flux, as indicated by the indigo (yellow) arrow. **d**, Probability distribution of the qubit frequency under Gaussian flux noise in the linear regime (yellow) vs. the quadratic regime (indigo). In the quadratic regime, the right-skewness of the distribution illustrates the non-Gaussianity of the resulting noise process.

lants of order $k \geq 3$ vanish identically. By contrast, for non-Gaussian noise, all cumulants can be non-zero in principle. Assuming that noise is stationary, so that the mean of the process, $\mathbb{E}[B(t)] = C^{(1)}(0) \equiv \mu_B$ is constant, the phase parameter may be written as $\phi(t) = \mu_B F_p(0, t) + \varphi(t)$, with the Fourier transform $F_p(\omega, t) \equiv \int_0^t ds e^{-i\omega s} y_p(s)$ being the fundamental filter function (FF) associated to the control [12]. This expression separates the phase due to the noise mean, which arises for both Gaussian and non-Gaussian noise, from a genuinely *non-Gaussian phase* $\varphi(t)$, which captures the contribution of all odd noise cumulants with $k \geq 3$. For sufficiently small time or noise strength, we can neglect terms of order $k > 3$ in the cumulant expansion, leading to

$$\chi(t) \approx \frac{1}{2\pi} \int_{\mathbb{R}} d\omega |F_p(\omega, t)|^2 S(\omega), \quad (1)$$

$$\varphi(t) \approx -\frac{1}{3!(2\pi)^2} \int_{\mathbb{R}^2} d\vec{\omega} G_p(\vec{\omega}, t) S_2(\vec{\omega}), \quad (2)$$

where $\vec{\omega} \equiv (\omega_1, \omega_2)$ and the second and third noise cumulants enter the qubit dynamics through their Fourier transforms: the PSD or spectrum, $S(\omega) \equiv \int_{\mathbb{R}} d\tau e^{-i\omega\tau} C^{(2)}(0, \tau)$, and the second-order polyspectrum or bispectrum, $S_2(\vec{\omega}) \equiv \int_{\mathbb{R}^2} d\vec{\tau} e^{-i\vec{\omega}\cdot\vec{\tau}} C^{(3)}(0, \tau_1, \tau_2)$, with $\vec{\tau} \equiv (\tau_1, \tau_2)$. In the frequency domain, the influence of such spectra is “filtered” by a corresponding generalized FF – in particular, $G_p(\vec{\omega}, t) \equiv F_p(-\omega_1, t) F_p(-\omega_2, t) F_p(\omega_1 + \omega_2, t)$ [12]. Since, to leading order, non-Gaussian features arise in our setting from $S_2(\vec{\omega})$, non-Gaussianity of a noise process will be detected and characterized through measurements of $\varphi(t)$.

Experimental setup and noise validation

Our circuit QED system [42, 43] contains an engineered flux qubit [44], which is designed to enable fast single-qubit gates with high fidelity at its flux degeneracy point ($F_g > 99.9\%$; see Supplementary Notes 1 and 2). Single-qubit operations are performed using cosine-shaped microwave pulses, applying an optimal-control technique to suppress leakage to higher levels [45]. Inductive coupling to a local antenna is used to modulate the external flux Φ threading the qubit loop interrupted by Josephson junctions (Fig. 1a and Fig. 1b). Near the degeneracy (or optimal [35]) point $\Phi = \Phi_0/2$, with Φ_0 the flux quantum, the $|0\rangle \rightarrow |1\rangle$ transition frequency ω_q has an approximately quadratic dependence on the external flux Φ (Fig. 1c). Hence, a sufficiently slow time-dependent external flux $\Phi(t)$ enables adiabatic modulation of the qubit frequency, leading to

$$B(t) = \beta_\Phi [\Delta\Phi(t)]^2, \quad \Delta\Phi(t) \equiv \Phi(t) - \Phi_0/2, \quad (3)$$

where β_Φ is the quadratic coefficient in the dispersion relation between qubit frequency and flux. Crucially, any non-linear function of a Gaussian process leads to non-Gaussian noise. In particular, the quadratic function implemented in Eq. (3) transduces zero-mean Gaussian flux noise into non-Gaussian qubit-frequency noise (Figs. 1c and d). Assuming that the noise is entirely contributed by the applied $\Delta\Phi(t)$, and that $S_\Phi(\omega)$ denotes the corresponding PSD, the mean μ_B , PSD $S(\omega)$, and bispectrum $S_2(\omega_1, \omega_2)$ of $B(t)$ are respectively given by

$$\mu_B = \frac{\beta_\Phi}{2\pi} \int_{\mathbb{R}} d\omega S_\Phi(\omega), \quad (4)$$

$$S(\omega) = \frac{\beta_\Phi^2}{\pi} \int_{\mathbb{R}} du S_\Phi(u) S_\Phi(\omega - u), \quad (5)$$

$$S_2(\omega_1, \omega_2) = \frac{4\beta_\Phi^3}{\pi} \int_{\mathbb{R}} du S_\Phi(u) S_\Phi(\omega_1 + u) S_\Phi(\omega_2 - u), \quad (6)$$

In the experiment, we choose $S_\Phi(\omega)$ to be a zero-mean Lorentzian function, $S_\Phi(\omega) = (P_0/\pi\omega_c)/[1+(\omega/\omega_c)^2]$, where $\omega_c/2\pi$ ($= 0.5$ MHz) and P_0 denote the cutoff frequency and the power of the applied flux noise, respectively. As is apparent from Eqs. (4)–(6), cumulants of order $k = 1, 2$, and 3 are distinguished by their linear, quadratic, and cubic dependence on power, respectively.

We first validate the intended engineered non-Gaussian noise by demonstrating consistency of the measured power dependence of χ and ϕ with the above prediction. The qubit is initialized to the $+y$ axis by applying a $\pi/2$ pulse about x (rotation $R_x(\pi/2)$), and Gaussian flux noise is injected while it evolves in the xy -plane of the Bloch sphere for time T . During this evolution, we apply a Carr-Purcell-Meiboom-Gill (CPMG) sequence consisting of two refocusing π pulses about y (Fig. 2a). At the end of this sequence ($t = T$), the effect of the first cumulant of the noise cancels out ($F_p(0, T) = 0$) and, as a result, the measured phase becomes solely determined by odd cumulants of order $k \geq 3$: $\phi(T) = \varphi(T)$. To estimate both ϕ and χ , we measure $\langle\sigma_x\rangle$ and $\langle\sigma_y\rangle$ by applying appropriate tomography pulses at time $t = T$, before readout in the σ_z -basis.

Figures 2b and 2c show χ and ϕ as a function of injected flux noise power P_0 for both the experiment (blue triangles) and Monte Carlo simulations accounting for all cumulants of the applied noise (orange squares, see Supplementary Note 5). Substituting Eqs. (5) and (6) into Eqs. (1) and (2), we also plot the resulting ideal weak-power behavior (gray solid) considering only the leading-order cumulants of order two and three

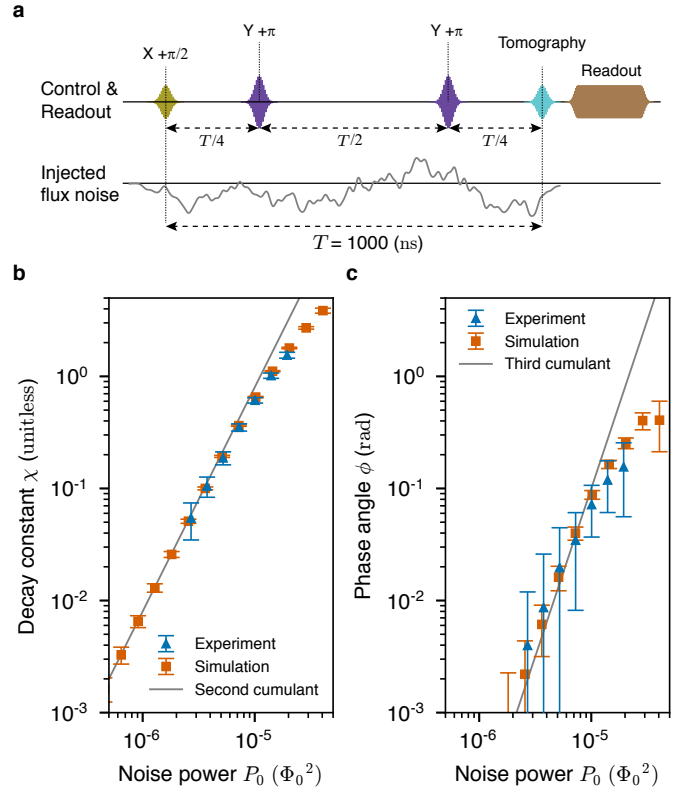


Figure 2. Power dependence of decay constant (χ) and phase angle (ϕ). **a**, Pulse scheme for measuring the power dependence of χ and ϕ , consisting of a CPMG sequence of length $T = 1 \mu\text{s}$ with two π pulses. Flux noise waveforms are temporally tailored to affect the qubit only while it evolves on the transverse plane. **b**, Decay constant $\chi = -\log(\sqrt{\langle\sigma_x\rangle^2 + \langle\sigma_y\rangle^2})$ and **c**, phase angle $\phi = \tan^{-1}(-\langle\sigma_x\rangle/\langle\sigma_y\rangle)$ at time $t = T$, after application of a CPMG sequence as a function of the applied noise power P_0 . A cubic power dependence of ϕ , for sufficiently weak noise, corroborates non-Gaussianity of the engineered noise. Error bars represent 95% confidence intervals.

for χ and ϕ , respectively. For sufficiently small P_0 , these ideal values are in good agreement with data from both experiment and simulation, showing that χ and ϕ obey the quadratic and cubic power dependences that are expected for the square of a Gaussian flux-noise process under the CPMG sequence. In particular, the cubic dependence of ϕ at small P_0 corroborates the presence of a non-zero third-order cumulant, which would not exist for Gaussian noise. Deviations of the simulations and experimental data from the ideal behavior at large P_0 are attributable to the contribution of cumulants of order $k > 3$. The quantitative agreement between theory, experiment, and simulation observed at low power demonstrates our capability to produce and sense engineered noise that dominates over native one over the relevant parameter regime and exhibits well controlled cumulants, a necessary first step in the experimental validation of non-Gaussian QNS.

Non-Gaussian noise spectroscopy

Having established that χ and ϕ follow their expected behavior, we move on to fully characterizing the first three cumulants of our engineered noise source by measuring its mean, PSD, and bispectrum. Since the noise mean, μ_B , manifests itself through a qubit-frequency shift, it can be measured from a simple parameter estimation scheme based on Ramsey interferometry. By contrast, we aim to perform a non-parametric estimation of both the PSD and bispectrum, that is, to recon-

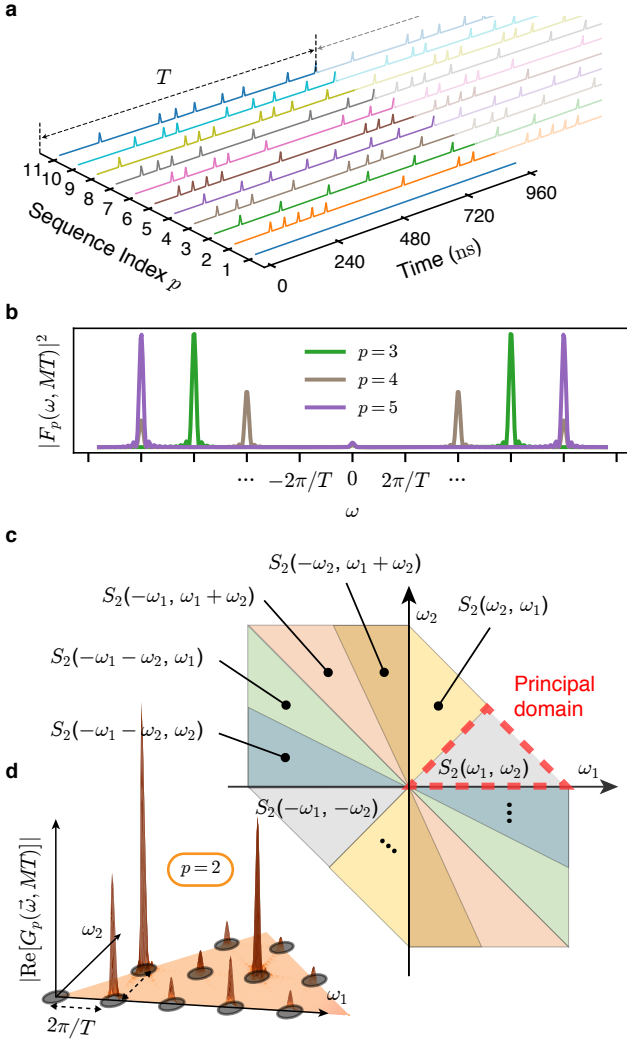


Figure 3. A protocol for non-Gaussian noise spectroscopy. **a**, Timing diagrams of control pulse sequences. The length of the base sequence is $T = 960$ ns, $p = 1$ corresponds to a single free-evolution period, whereas sequences $p = 2, \dots, 11$ are repeated $M = 10$ times. Only π -pulses are shown and all π -pulses are around the y -axis (see Supplementary Note 4 for details). **b**, $|F_p(\omega, MT)|^2$ for $p = 3, 4, 5$ as a function of angular frequency ω . **c**, Symmetries of the bispectrum of a classical stationary noise process. **d**, 2D grid representing the harmonic frequencies (black circles) in the principal domain \mathcal{D}_2 (orange area) in which the bispectrum is sampled. The amplitude of the relevant contribution of the FF in \mathcal{D}_2 , $|\text{Re}[G_p(\vec{\omega}, MT)]|$, for $p = 2$, (red surface plot) is shown on top of the grid.

construct them at a set of discrete points in frequency space without assuming a prior functional form. Figure 3 illustrates our protocol for simultaneous estimation of the PSD and bispectrum, in which filter design – the selection of pulse times in a control sequence so that the corresponding FF has a particular shape – is instrumental. Building on Ref. [13], applying $M \gg 1$ repetitions of a “base” pulse sequence $p \in \{1, 2, \dots, P\}$, with duration T , shapes the FF $|F_p(\omega, MT)|^2$ into a frequency comb with narrow teeth probing $S(\omega)$ at harmonics $k\omega_h$, with k an integer and $\omega_h \equiv 2\pi/T$ (Figs. 3a and b). This result generalizes to filters relevant to higher-order spectra [12]: under sequence repetition, $G_p(\vec{\omega}, MT)$ becomes a two-dimensional (2D) “hyper-comb” with teeth probing $S_2(\vec{\omega})$ at $\vec{\omega} \in \{\vec{k}\omega_h\}$, where $\vec{k} \equiv (k_1, k_2)$ with k_1 and k_2 integers (Fig. 3d).

For both the PSD and bispectrum, distinct pulse sequences have the effect of giving different weights to the comb teeth, granting access to complementary information about $S(k\omega_h)$

and $S_2(\vec{k}\omega_h)$, enabling their reconstruction. More specifically, in both cases the basic steps of our protocol consist of (i) applying a set of sufficiently distinct pulse sequences p (Fig. 3a); (ii) measuring the corresponding decay and phase parameters; and (iii) solving the resulting systems of linear equations, which give $\chi_p(MT)$ and $\varphi_p(MT)$ as a function of $S(k\omega_h)$ and $S_2(\vec{k}\omega_h)$. Since classical noise has a spectrum with even symmetry, $S(\omega) = S(-\omega)$, the PSD is specified across all frequency space by its values at positive frequencies. Likewise, the bispectrum is completely specified by its values over a subspace \mathcal{D}_2 known as the principal domain [41, 46], illustrated in Fig. 3d. Reconstructing the bispectrum over \mathcal{D}_2 and exploiting the symmetries that $S_2(\vec{\omega})$ exhibits (shown in Fig. 3c) thus suffices to retrieve the bispectrum over the whole relevant frequency domain.

Figure 4 presents experimental results for determining the mean and PSD, which suffice to characterize the noise process in the Gaussian approximation. To measure μ_B by Ramsey interferometry, we apply a pair of $\pi/2$ pulses with a drive at frequency ω_d , first about x at time $t = 0$ ($R_x(\pi/2)$), and then about y at time $t = T$ ($R_y(\pi/2)$). We choose a pulse interval $T = 50$ ns, which is short enough for cumulants of order higher than one to be negligible, but long enough to avoid pulse overlap. The qubit polarization at time t_f after the two pulses is then $\langle \sigma_z(t_f) \rangle \approx (D + \mu_B)T'$, where $D \equiv \omega_q - \omega_d$ is the drive detuning, and T' is an effective time interval that accounts for the finite-width pulse shape (see Supplementary Note 6). Thus, plotting $\langle \sigma_z(t_f) \rangle$ as a function of D produces a straight line whose x -intercept is $-\mu_B$, leading to an estimate that is insensitive to the pulse shape to first order in the cumulant expansion. Figure 4a presents data for measurements of $\langle \sigma_z(t_f) \rangle$, and shows how we isolate the contribution of the engineered noise source by performing the sequence with (blue data set) and without (black data set) applied noise. The mean of the engineered noise is estimated by subtracting the x -intercepts of the straight lines that are fitted to each data set. Performing these fits under the conditional normal model of linear regression (see Supplementary Note 6) yields the estimate $\mu_B^{\text{est}}/2\pi = 127.1 \pm 7.56$ kHz, where the uncertainty corresponds to the 95% confidence interval calculated from the asymptotic normal distribution of qubit polarization.

To estimate the PSD by the comb approach outlined above, we use both a period of free evolution ($p = 1$) and $M = 10$ repetitions of base sequences $p = 2, \dots, 11$ illustrated in Fig. 3a (see Supplementary Note 4 for the actual pulse times). For $M \gg 1$, the FF entering the decay constant in Eq. (1) becomes approximately $|F_p(\omega, MT)|^2 \approx \frac{M}{T} |F_p(\omega, T)|^2 \sum_{k=-\infty}^{\infty} \delta(\omega - k\omega_h)$, which enables us to sample the PSD at the harmonic frequencies in terms of the (known) control FFs,

$$\chi_p(MT) \approx \frac{M}{T} \sum_{k \in \mathcal{K}_1} |F_p(k\omega_h, T)|^2 S(k\omega_h). \quad (7)$$

Here, we have used the even symmetry of the PSD, and the high-frequency decay of the PSD and FFs to truncate the comb to a finite set of positive harmonics, $\mathcal{K}_1 \equiv \{0, \dots, K-1\}$. Rather than solving the above linear system by matrix inversion as in Ref. [13], we employ a statistically-motivated maximum likelihood estimate (MLE), which takes experimental error into account (see Supplementary Note 7). Using measurements of $\chi_p(MT)$ for each of the same $P = 11$ control sequences to be

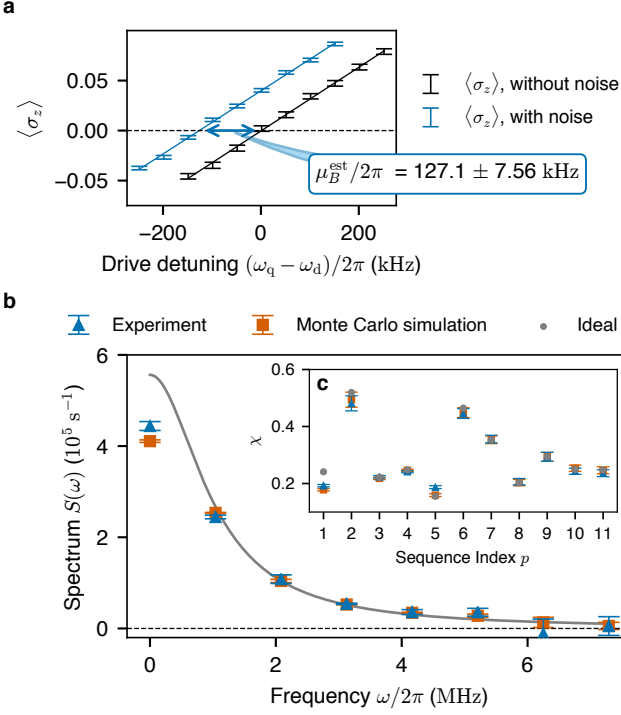


Figure 4. Gaussian spectral estimation: noise mean and PSD. **a**, Measured values of $\langle \sigma_z \rangle$ after a 50 ns-long Ramsey sequence vs. drive detuning $D = \omega_q - \omega_d$. The separation between the x -intercepts of the two fitted lines gives the mean μ_B^{est} of the injected dephasing noise. **b**, Comparison of the experimental reconstruction (blue triangle) and Monte Carlo simulation (orange square) with the ideal PSD (gray solid line). **c**, Decay constants χ . Except for $p = 1$, the ideal data (gray circles) are in very good agreement with both the experimental results and Monte Carlo simulations. Error bars represent 95% confidence intervals.

used for the bispectrum estimation, we find a well-conditioned system for $K = 8$.

Figure 4b compares the experimentally estimated PSD at the $K = 8$ harmonics (blue triangles) with the ideal PSD obtained from Eq. (5) for our engineered noise (solid gray line) and Monte Carlo simulations of the QNS protocol (orange squares). The experimental and simulated estimates of the PSD are plotted along with 95% confidence intervals obtained from the asymptotic normal distribution of the decay constants. Figure 4c shows the experimental and simulated values of $\chi_p(MT)$ that were used as input for the reconstructions, along with ideal values obtained by substituting Eq. (5) into Eq. (1) and approximating the FF by the ideal (infinite) comb as given above. The PSD is slightly underestimated at zero frequency in both the experiment and Monte Carlo simulation since the FF of sequence $p = 1$ (a 1 μs -long free induction decay) is comparable in bandwidth to the PSD, whereas the reconstruction procedure assumes the PSD is sampled by infinitely narrow FFs. The disagreement of the experimental and simulated $\chi_p(MT)$ for $p = 1$ with the ideal value is also explained by the non-negligible bandwidth of the FF (Fig. 4c). Apart from these well-understood discrepancies at $\omega = 0$, the quantitative agreement of the experimental reconstruction with simulations and ideal values is remarkable, which demonstrates that our protocol is able to reliably characterize Gaussian features of the applied noise.

We are now in a position to present our key result: the reconstruction of the noise bispectrum. As anticipated, this entails a higher-dimensional analogue of the comb-based ap-

proach used for the PSD. We estimate the non-Gaussian phase given in Eq. (2) by subtracting the contribution of the noise mean from the total measured phase, $\varphi_p(MT) = \phi_p(MT) - \mu_B F_p(0, MT)$, where we replace μ_B by μ_B^{est} experimentally determined above. After $M \gg 1$ repetitions of sequence p , the FF becomes a 2D comb (Fig. 3d), and the non-Gaussian phase becomes a sampling of the bispectrum at the harmonics $k\omega_h$, that is, $\varphi_p(MT) = -\frac{M}{3!T^2} \sum_{\vec{k} \in \mathcal{Z}^2} G_p(\omega_h \vec{k}, T) S_2(\omega_h \vec{k})$. Since both the filter and bispectrum decay at high frequencies, we can truncate this sum to a finite number of $\vec{k} = (k_1, k_2)$. As the bispectrum is completely specified by its values on the principal domain, we may further restrict our consideration to a subset of harmonics, $\mathcal{K}_2 \equiv \{\vec{k}_1, \dots, \vec{k}_N\} \subset \mathcal{D}_2$ (Fig. 3c). The non-Gaussian phase then becomes

$$\varphi_p(MT) = -\frac{M}{3!T^2} \sum_{\vec{k} \in \mathcal{K}_2} m(\omega_h \vec{k}) \text{Re}[G_p(\omega_h \vec{k}, T)] S_2(\omega_h \vec{k}), \quad (8)$$

where the multiplicity $m(\omega_h \vec{k})$ accounts for the number of points equivalent to $S_2(\omega_h \vec{k})$ by the symmetry properties of the bispectrum. Also on account of these symmetries, the imaginary component of $G_p(\omega_h \vec{k}, T)$ cancels when the sum is restricted to \mathcal{D}_2 (see Supplementary Note 8).

By measuring the non-Gaussian phase for $P \geq N$ different control sequences, we can construct a vector $\vec{\varphi} = [\varphi_1(MT), \dots, \varphi_P(MT)]^T$ and a linear system of the form

$$\vec{\varphi} = \mathbf{A} \vec{S}_2, \quad \mathbf{A}_{pn} = -\frac{M}{3!T^2} m(\omega_h \vec{k}_n) \text{Re}[G_p(\omega_h \vec{k}_n, T)], \quad (9)$$

where $\vec{S}_2 = [S_2(\omega_h \vec{k}_1), \dots, S_2(\omega_h \vec{k}_N)]^T$ contains the bispectrum at the harmonics in \mathcal{K}_2 and \mathbf{A} is a $P \times N$ reconstruction matrix. The simplest way to estimate the bispectrum from this linear system is the least-squares estimate employed in Ref. [41], involving the (pseudo-)inverse of the reconstruction matrix, $\vec{S}_2^{\text{est}} = \mathbf{A}^{-1} \vec{\varphi}$. As in the case of PSD estimation, a potential drawback of this inversion-based approach is numerical instability stemming from an ill-conditioned \mathbf{A} , which occurs when the FFs have a high degree of spectral overlap. Since ill-conditioning makes the least-squares estimate sensitive to even small errors in the measured phases, we again utilize a maximum-likelihood approach with optional regularization to further increase stability (see Supplementary Note 8). From the asymptotic Gaussian distribution of the measurement outcomes of $\vec{\varphi}$, the regularized maximum-likelihood estimate (RMLE) is found as

$$\vec{S}_2^{\text{RMLE}} = \underset{\vec{S}_2}{\text{argmin}} \left[\frac{1}{2} (\mathbf{A} \vec{S}_2 - \vec{\varphi})^T \mathbf{\Sigma}^{-1} (\mathbf{A} \vec{S}_2 - \vec{\varphi}) + \|\lambda \mathbf{D} \vec{S}_2\|_2^2 \right], \quad (10)$$

where $\|\cdot\|_2$ denotes the L_2 -norm and $\lambda \geq 0$ parametrizes the strength of the regularization [47]. Due to its dependence on the covariance matrix $\mathbf{\Sigma}$, the RMLE down-weights phase measurements with larger error. Numerical stability is increased by the regularizer $\|\lambda \mathbf{D} \vec{S}_2\|_2^2$, which acts as an effective constraint. When the smoothing matrix \mathbf{D} is proportional to \mathbf{I} , the regularizer reduces to the well-known Tikhonov (or L_2) form. Since the numerical stability afforded by regularization comes at the cost of additional bias, choosing the regularization strength is a nontrivial task. In Supplementary Note 8, we detail how we

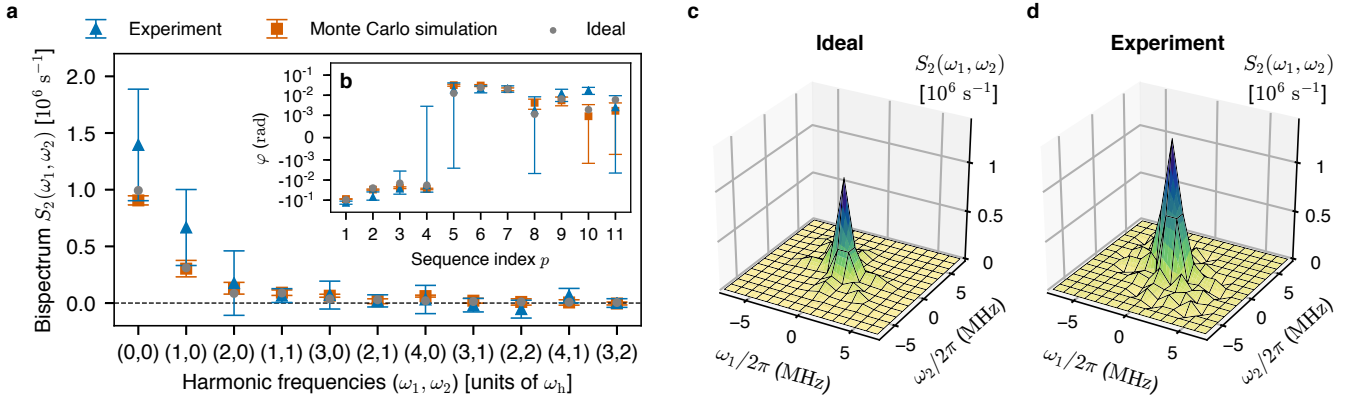


Figure 5. Non-Gaussian spectral estimation: noise bispectrum. **a**, Experimental data (blue triangles), Monte Carlo simulations (orange squares) and ideal values (gray circles) for the bispectrum of the engineered dephasing noise. The error bars indicate that the experimental bispectrum agrees with both the ideal bispectrum and Monte Carlo simulations of the protocol within 95% confidence intervals. **b**, Estimated non-Gaussian phase angles φ . Error bars represent 95% confidence intervals. **c**, 3D visualization of the ideal bispectrum. **d**, 3D visualization of the reconstructed bispectrum for the experimental data.

have selected λ based on the so-called ‘‘L-curve criterion’’. Interestingly, since \mathbf{A} is sufficiently well-conditioned for the sequences we have chosen, we find that regularization gives negligible benefit. Accordingly, we use $\lambda = 0$ (which recovers standard MLE) in our experimental reconstructions.

Figure 5a compares the results of the non-Gaussian spectral estimation for the harmonics in the principal domain for the experiment (blue triangles) with both the ideal bispectrum obtained from Eq. (6) (gray circles) and from Monte Carlo simulations (orange squares). To estimate the experimental bispectrum, we input the measured data for $\vec{\varphi}$ and Σ shown in Fig. 5b into \vec{S}_2^{RMLE} given by Eq. (10). The ideal values of φ_p , also shown in Fig. 5b, are obtained by substituting Eq. (6) into Eq. (2). We further display 3D representations of the full bispectra, obtained by applying relevant symmetries to the data on \mathcal{D}_2 , for the ideal (Fig. 5c) and experimental (Fig. 5d) cases, respectively. Ignoring error bars, the reconstructed bispectrum appears to be an over-estimate with respect to the ideal one. This error may be attributed to noise during the finite-duration control pulses used in the experiment, leading to effective pulse infidelity. Upon taking the error bars in Fig. 5a into consideration, however, the ideal and simulated values of the bispectrum lie within the 95% confidence intervals of the experimental reconstruction, suggesting that this estimation error is statistically insignificant and thus successfully extending the validation of our QNS protocol to the leading non-Gaussian noise cumulant.

Although the theoretical bispectrum falls within the 95% confidence interval of the estimate, reducing the magnitude of uncertainties is clearly necessary to push the application of non-Gaussian QNS to uncontrollable native noise, whose strength may be comparatively weak. We note that the spectral characterization of the non-Gaussian noise process engineered in this experiment requires an extremely precise estimation of μ_B . Since reconstructions of the bispectrum are obtained using $\varphi_p(MT) = \phi_p(MT) - \mu_B F_p(0, MT)$, the uncertainty in μ_B^{est} propagates to $\varphi_p(MT)$ when p has zero filter order, i.e. $F_p(0, MT) \neq 0$. These sequences play a crucial role in estimating the bispectrum at the ‘‘zero points’’, grid points (ω_1, ω_2) with $\omega_1 = 0$ or $\omega_2 = 0$. Since μ_B is much larger than the third cumulant for the current noise process, even a small relative uncertainty in μ_B^{est} can lead to greater error in the bispectrum estimate at the zero points, as the error bars in Fig. 5a attest.

Discussion

In summary, we reported the first experimental demonstration of high-order spectral estimation in a quantum system. By producing and sensing engineered noise with well-controlled cumulants, we were able to successfully validate a spectroscopy protocol that reconstructs both the power spectral density and the bispectrum of non-Gaussian dephasing noise. Our theory and experimental demonstration lay the groundwork for future research aiming at complete spectral characterization of realistic non-Gaussian noise environments in quantum devices and materials. Theoretically, we expect that the regularized maximum-likelihood estimation approach to quantum noise spectroscopy we invoked here will prove crucial to ensure stable spectral reconstructions in more general settings. Devising alternative estimation protocols based on optimally band-limited control modulation and multitaper techniques [48] appears especially compelling, in view of recent advances in the Gaussian regime [24, 49]. We believe that obtaining a complete spectral characterization will ultimately provide deeper insight into the physics and interplay of different microscopic noise mechanisms, including non-classical non-Gaussian noise, as possibly arising from photon-number mediated non-linear couplings [50].

Data availability

The data that support the findings of this study may be made available from the corresponding authors upon request and with the permission of the US Government sponsors who funded the work.

Code availability

The code used for the analyses may be made available from the corresponding authors upon request and with the permission of the US Government sponsors who funded the work.

References

1. Percival, D. B. & Walden, A. T. *Spectral Analysis for Physical Applications* (Cambridge University Press, 1993).
2. Preskill, J. Quantum Computing in the NISQ era and beyond. *Quantum*, **79** (2018).
3. Sekatski, P., Skotiniotis, M. & Dür, W. Dynamical decoupling leads to improved scaling in noisy quantum metrology. *New J. Phys.* **18**, 073034 (2016).
4. Beaudoin, F., Norris, L. M. & Viola, L. Ramsey interferometry in correlated quantum noise environments. *Phys. Rev. A* **98**, 020102(R) (2018).
5. Preskill, J. Sufficient condition on noise correlations for scalable quantum computing. *Quantum Inf. Comput.* **13**, 181–194 (2013).
6. Schoelkopf, R. J., Clerk, A. A., Girvin, S. M., Lehnert, K. W. & Devoret, M. H. *Qubits as spectrometers of quantum noise* in in: *Quantum Noise in Mesoscopic Physics*, NATO Science Series **97** (Springer, Dordrecht, 2002), 175–203.
7. Faoro, L. & Viola, L. Dynamical suppression of $1/f$ noise processes in qubit systems. *Phys. Rev. Lett.* **92**, 117905 (2004).
8. Cywiński, L., Lutchyn, R. M., Nave, C. P. & Das Sarma, S. How to enhance dephasing time in superconducting qubits. *Phys. Rev. B* **77**, 174509 (2008).
9. Biercuk, M. J. *et al.* Optimized dynamical decoupling in a model quantum memory. *Nature* **458**, 996–1000 (2009).
10. Yuge, T., Sasaki, S. & Hirayama, Y. Measurement of the noise spectrum using a multiple-pulse sequence. *Phys. Rev. Lett.* **107**, 170504 (2011).
11. Young, K. C. & Whaley, K. B. Qubits as spectrometers of dephasing noise. *Phys. Rev. A* **86**, 012314 (2012).
12. Paz-Silva, G. A. & Viola, L. General transfer-function approach to noise filtering in open-loop quantum control. *Phys. Rev. Lett.* **113**, 250501 (2014).
13. Álvarez, G. A. & Suter, D. Measuring the spectrum of colored noise by dynamical decoupling. *Phys. Rev. Lett.* **107**, 230501 (2011).
14. Bylander, J. *et al.* Noise spectroscopy through dynamical decoupling with a superconducting flux qubit. *Nature Phys.* **7**, 565–570 (2011).
15. Yan, F. *et al.* Rotating-frame relaxation as a noise spectrum analyser of a superconducting qubit undergoing driven evolution. *Nature Commun.* **4**, 2337 (2013).
16. Yoshihara, F. *et al.* Flux qubit noise spectroscopy using Rabi oscillations under strong driving conditions. *Phys. Rev. B* **89**, 020503(R) (2014).
17. Quintana, C. M. *et al.* Observation of classical-quantum crossover of $1/f$ flux noise and its paramagnetic temperature dependence. *Phys. Rev. Lett.* **118**, 057702 (2017).
18. Dial, O. E. *et al.* Charge noise spectroscopy using coherent exchange oscillations in a singlet-triplet qubit. *Phys. Rev. Lett.* **110**, 146804 (2013).
19. Muhonen, J. T. *et al.* Storing quantum information for 30 seconds in a nanoelectronic device. *Nature Nanotech.* **9**, 986–991 (2014).
20. Chan, K. W. *et al.* Assessment of a silicon quantum dot spin qubit environment via noise spectroscopy. *Phys. Rev. Applied* **10**, 044017 (2018).
21. Yoneda, J. *et al.* A quantum-dot spin qubit with coherence limited by charge noise and fidelity higher than 99.9%. *Nature Nanotech.* **13**, 102–107 (2018).
22. Meriles, C. A. *et al.* Imaging mesoscopic nuclear spin noise with a diamond magnetometer. *J. Chem. Phys.* **133**, 124105 (2010).
23. Romach, Y. *et al.* Spectroscopy of surface-induced noise using shallow spins in diamond. *Phys. Rev. Lett.* **114**, 017601 (2015).
24. Frey, V. M. *et al.* Application of optimal band-limited control protocols to quantum noise sensing. *Nature Comms.* **8**, 2189 (2017).
25. Wang, Y. *et al.* Single-qubit quantum memory exceeding ten-minute coherence time. *Nature Photon.* **11**, 646–650 (2017).
26. Paladino, E., Galperin, Y. M., Falci, G. & Altshuler, B. L. $1/f$ noise: Implications for solid-state quantum information. *Rev. Mod. Phys.* **86**, 361–418 (2014).
27. Simmonds, R. W. *et al.* Decoherence in Josephson phase qubits from junction resonators. *Phys. Rev. Lett.* **93**, 077003 (2004).
28. Oliver, W. D. & Welander, P. B. Materials in superconducting quantum bits. *MRS Bulletin* **38**, 816–825 (2013).
29. Zaretsky, V., Suri, B., Novikov, S., Wellstood, F. C. & Palmer, B. S. Spectroscopy of a Cooper-pair box coupled to a two-level system via charge and critical current. *Phys. Rev. B* **87**, 174522 (2013).
30. Lisenfeld, J. *et al.* Observation of directly interacting coherent two-level systems in an amorphous material. *Nature Commun.* **6**, 6182 (2015).
31. Lisenfeld, J. *et al.* Spectroscopy of a Cooper-pair box coupled to a two-level system via charge and critical current. *Sci. Rep.* **6**, 23786 (2016).
32. Falci, G., D’Arrigo, A., Mastellone, A. & Paladino, E. Dynamical suppression of telegraph and $1/f$ noise due to quantum bistable fluctuators. *Phys. Rev. A* **70**, 040101 (2004).
33. Galperin, Y. M., Altshuler, B. L., Bergli, J., Shantsev, D. & Vinokur, V. Non-Gaussian dephasing in flux qubits due to $1/f$ noise. *Phys. Rev. B* **76**, 064531 (2007).
34. Kotler, S., Akerman, N., Glickman, Y. & Ozeri, R. Non-linear single-spin spectrum analyzer. *Phys. Rev. Lett.* **110**, 110503 (2013).
35. Makhlin, Y. & Shnirman, A. Dephasing of solid-state qubits at optimal points. *Phys. Rev. Lett.* **92**, 178301 (2004).
36. Barends, R. *et al.* Superconducting quantum circuits at the surface code threshold for fault tolerance. *Nature* **508**, 500–503 (2014).
37. Yan, F. *et al.* The flux qubit revisited to enhance coherence and reproducibility. *Nature Commun.* **7**, 12964 (2016).
38. Hutchings, M. D. *et al.* Tunable superconducting qubits with flux-independent coherence. *Phys. Rev. Applied* **8**, 044003 (2017).

39. Lin, Y.-H. *et al.* Demonstration of protection of a superconducting qubit from energy decay. *Phys. Rev. Lett.* **120**, 150503 (2018).
 40. Nikias, C. L. & Mendel, J. M. Signal processing with higher-order spectra. *IEEE Signal Proc. Mag.* **10**, 10–37 (1993).
 41. Norris, L. M., Paz-Silva, G. A. & Viola, L. Qubit noise spectroscopy for non-Gaussian dephasing environments. *Phys. Rev. Lett.* **116**, 150503 (2016).
 42. Blais, A., Huang, R. S., Wallraff, A., Girvin, S. M. & Schoelkopf, R. J. Cavity quantum electrodynamics for superconducting electrical circuits: An architecture for quantum computation. *Phys. Rev. A* **69**, 062320 (2004).
 43. Wallraff, A. *et al.* Strong coupling of a single photon to a superconducting qubit using circuit quantum electrodynamics. *Nature* **431**, 162–167 (2004).
 44. Yan, F. *et al.* Principles for optimizing generalized superconducting flux qubit design. *in preparation* (2019).
 45. Motzoi, F., Gambetta, J. M., Rebentrost, P. & Wilhelm, F. K. Simple pulses for elimination of leakage in weakly nonlinear qubits. *Phys. Rev. Lett.* **103**, 110501 (2009).
 46. Chandran, V. & Elgar, S. A general procedure for the derivation of principal domains of higher-order spectra. *IEEE Trans. Signal Proc.* **42**, 229–233 (1994).
 47. Hansen, P. C. *The L-curve and its use in the numerical treatment of inverse problems in Computational Inverse Problems in Electrocardiology* (WIT Press, 2000), 119–142.
 48. Birkelund, Y., Hanssen, A. & Powers, E. J. Multitaper estimators of polyspectra. *Signal Proc.* **83**, 545–559 (2003).
 49. Norris, L. M. *et al.* Optimally band-limited spectroscopy of control noise using a qubit sensor. *Phys. Rev. A* **98**, 032315 (2018).
 50. Yan, F. *et al.* Distinguishing coherent and thermal photon noise in a circuit quantum electrodynamical system. *Phys. Rev. Lett.* **120**, 260504 (2018).
- L.V., L.M.N., S.G. and W.D.O. provided feedback. L.M.N., F.B., and L.V. designed the pulse sequences and developed the estimation protocol used in the experiment. F.Y. and S.G. designed the device and D.K.K. and J.L.Y. fabricated it. J.Y.Q. and U.L. provided experimental assistance. Y.S., F.B., L.M.N., and L.V. wrote the manuscript with feedback from all authors. L.V., S.G., T.P.O., and W.D.O. supervised the project.

Competing Interests

The authors declare no competing interests.

Acknowledgement

It is a pleasure to thank K. Harrabi, M. Kjaergaard, P. Krantz, G. A. Paz-Silva, J.I.J. Wang, and R. Winik for insightful discussions, and M. Pulido for generous assistance. We thank H. Bethany for the SEM image of the device. This research was funded by the U.S. Army Research Office grant No. W911NF-14-1-0682 (to L.V. and W.D.O.); and by the Department of Defense via MIT Lincoln Laboratory under Air Force Contract No. FA8721-05-C-0002 (to W.D.O.). Y.S. and F. B. acknowledge support from the Korea Foundation for Advanced Studies and from the Fonds de Recherche du Québec – Nature et Technologies, respectively. The views and conclusions contained herein are those of the authors and should not be interpreted as necessarily representing the official policies or endorsements, either expressed or implied, of the U.S. Government.

Author contribution

Y.S., F.Y., and S.G. performed the experiments. F.B. and Y.S. carried out numerical simulations and analyzed the data and

Supplementary Information

1 Additional experimental and computational detail

1.1 Device parameters and fabrication of the qubit sensor

Device parameters are summarized in Table S1.

Table S1. Device parameters.

Parameter	Value
Qubit frequency $\omega_0/2\pi$	2.920 GHz
Qubit anharmonicity $A/2\pi$	1.163 GHz
Relaxation time T_1	$27.0 \pm 2.7 \mu\text{s}$
Spin-echo relaxation time T_2	$35.9 \pm 4.4 \mu\text{s}$
Free induction decay time T_2^*	$12.2 \pm 1.0 \mu\text{s}$
Readout cavity frequency $\omega_r/2\pi$	7.348 GHz
Readout cavity linewidth $\kappa/2\pi$	2.548 MHz
Dispersive coupling strength $\chi/2\pi$	0.130 MHz

The device was fabricated in the same way as in Ref. [37]. It is a generalized version of the capacitively shunted flux qubit [37], comprising a capacitively shunted small-area junction in parallel is a series array of N junctions. In the capacitively shunted flux qubit of Ref. [37], this array comprised $N = 2$ junctions. Here, the number of array junctions is $N = 8$, far fewer than used in the fluxonium regime of operation [S1]. The area of each Josephson junction forming the array is identical and designed to be $0.2 \times 1.2 \mu\text{m}^2$. The left junction in Fig. 1a is smaller in area by a factor of 8 than the right junction ($\alpha = 1/8$). The critical current density J_c is measured to be $0.60 \pm 0.01 \mu\text{A}/\mu\text{m}^2$ and the shunt capacitance C_{sh} is designed to be 20 fF.

1.2 Randomized benchmarking of single-qubit gates

We characterized an average error rate of single-qubit gates by performing Clifford randomized benchmarking [S2] (Fig. S1). As mentioned in the main text, single-qubit operations are performed using cosine-shaped microwave pulses, applying a quadrature correction (DRAG [45]) to minimize unwanted phase evolution and leakage due to the presence of higher levels.

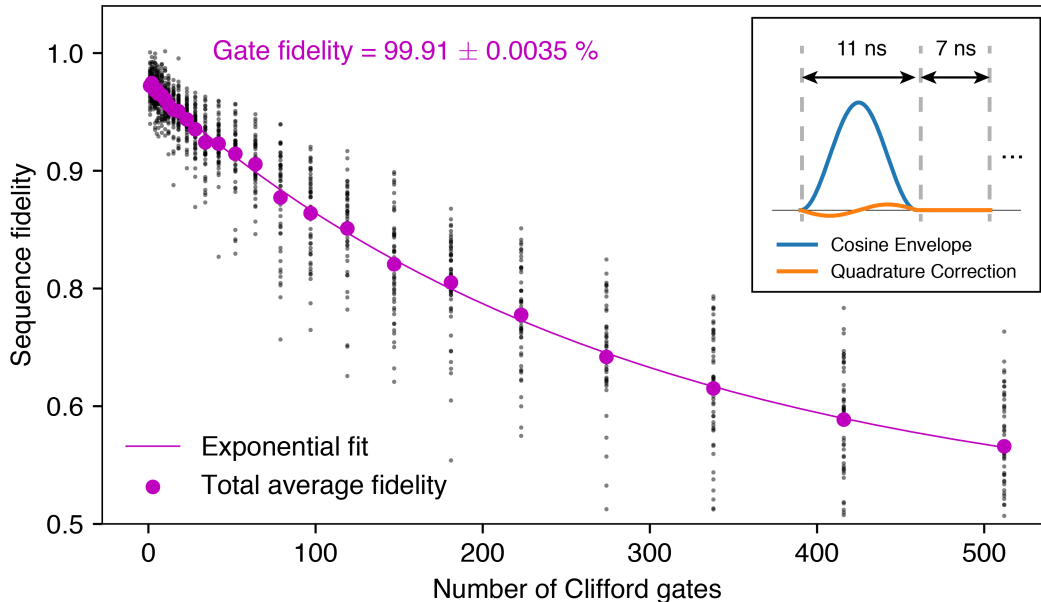


Figure S1. Randomized benchmarking of single-qubit gates. Standard single-qubit Clifford randomized benchmarking, indicated as average sequence fidelity (magenta circle) vs. number of Clifford gates. There are 50 randomizations for each number of Clifford gates. The envelope of microwave pulse is a cosine with a total length of 11 ns; a constant buffer time of 7 ns is inserted after each pulse to ensure complete separation of the pulses (inset).

1.3 Measurement setup

1.3.1 Cryogenic setup

The experiments were performed using a Leiden CF-450 dilution refrigerator, capable of cooling to a base temperature of 15 mK. The samples were magnetically shielded with a superconducting can surrounded by a Cryoperm-10 cylinder. The schematic

of the cryogenic circuitry is shown in Figure S2. There are two RF lines for the input and the output of the samples; applying microwave readout tone and measuring the transmission of sample respectively. Thermal noise from room temperature on the RF drive lines is attenuated with 20 dB at the 3 K stage, followed by 6 dB at still, and 26 dB at the 20 mK stage. All attenuators in the cryogenic samples are made by XMA. Note that there is one additional RF line for pumping the Josephson traveling wave parametric amplifier (JTWPA) [S3] used as a first-stage pre-amplifier to amplify the readout signal at base temperature. The effective noise temperature is determined primarily by the JTWPA, with a total system noise measured to be about 600 mK. To avoid any back-action of the pump-signal from TWPA, we added a microwave isolator between the samples and the TWPA. On the RF output line, there is a high-electron mobility transistor (HEMT) amplifier (Cryo-1-12 SN508D) at the 3 K stage. Two microwave isolators allow for the signal to pass through to the amplifier without being attenuated, while taking all the reflected noise off of the amplifier and dumping it in a $50\ \Omega$ termination instead of reaching the sample.

There are two additional lines for qubit flux bias: one is for DC flux bias, which is applied globally through a coil installed in the device package, the other is to apply magnetic flux to the qubit thorough a local antenna. The primary requirement of the DC flux bias line is the ability to tune through at least a single flux quantum on the SQUID of the qubit with high precision and low noise. The local flux bias line is attenuated by 20 dB at the 3 K stage, 6 dB at the still, 20 dB at the 20 mK stage to remove excess thermal photons from higher-temperature stages.

1.3.2 Room temperature control

Outside of the cryostat, we have all of the control components which allow us to apply microwave signals that address the cavity and the qubits, as well as the components necessary to resolve the readout signal. All the signals are added using microwave power splitters (Marki PD0R413) used in reverse. Direct digital synthesis of the qubit signals is performed using a high-speed arbitrary waveform generator (AWG Keysight M8195A), which has a 65 GS/sec sampling rate and sufficient bandwidth for this purpose. The output line is further amplified outside of the cryostat with an amplifier (MITEQ AMF-5D-00101200-23-10P) with a quoted noise figure of 2.3 dB, and a preamplifier (Stanford Research SR445A). A detailed schematic is given in Fig S2. We use an IQ demodulation technique to mix down the signal entering the RF port with a reference signal detuned by 40 MHz applied to the LO port. This results in down-converted signals to 40 MHz using a mixer. All components are frequency-locked via a common SRS rubidium frequency standard (10 MHz).

1.3.3 Pulse generation

Qubit control pulse generation is performed via a Keysight M8195A AWG. The pulses are programmed in Labber and then uploaded to the Keysight M8195A.

- Component List**
- Keysight M8195A
 - Keysight M3202A
 - Keysight M3202A
 - Agilent E8267D
 - Acquiris U1084A
 - BNC 845
 - Mini Circuits VLFX-300+
 - Marki PD-0R413
 - BNC 845 (Internal I/Q mixer)
 - SRS SR445A
 - Mini Circuits ZVE-8G+
 - Mini Circuits VLF-5500+
 - Mini Circuits VLFX-80+
 - Marki IR 4509 LXP
 - Yokogawa GS200
 - Mini Circuits BLP-1.9+
 - MITEQ AMF-5D-00101200-23-10P
 - Caltech Cryo-1-12 SN508D
 - Custom-made RC filter
 - RLC Electronics F-18948
 - RLC Electronics F-30-12.4-R
 - Quinstar QCI-075900XM00
 - Marki C20-0116
 - Radiall R591763600
 - Teledyne CCR-33S60-N
- * Components 1-6 are frequency-locked via a common SRS rubidium frequency standard (10MHz).
- * All attenuators inside the cryostat are made by XMA.

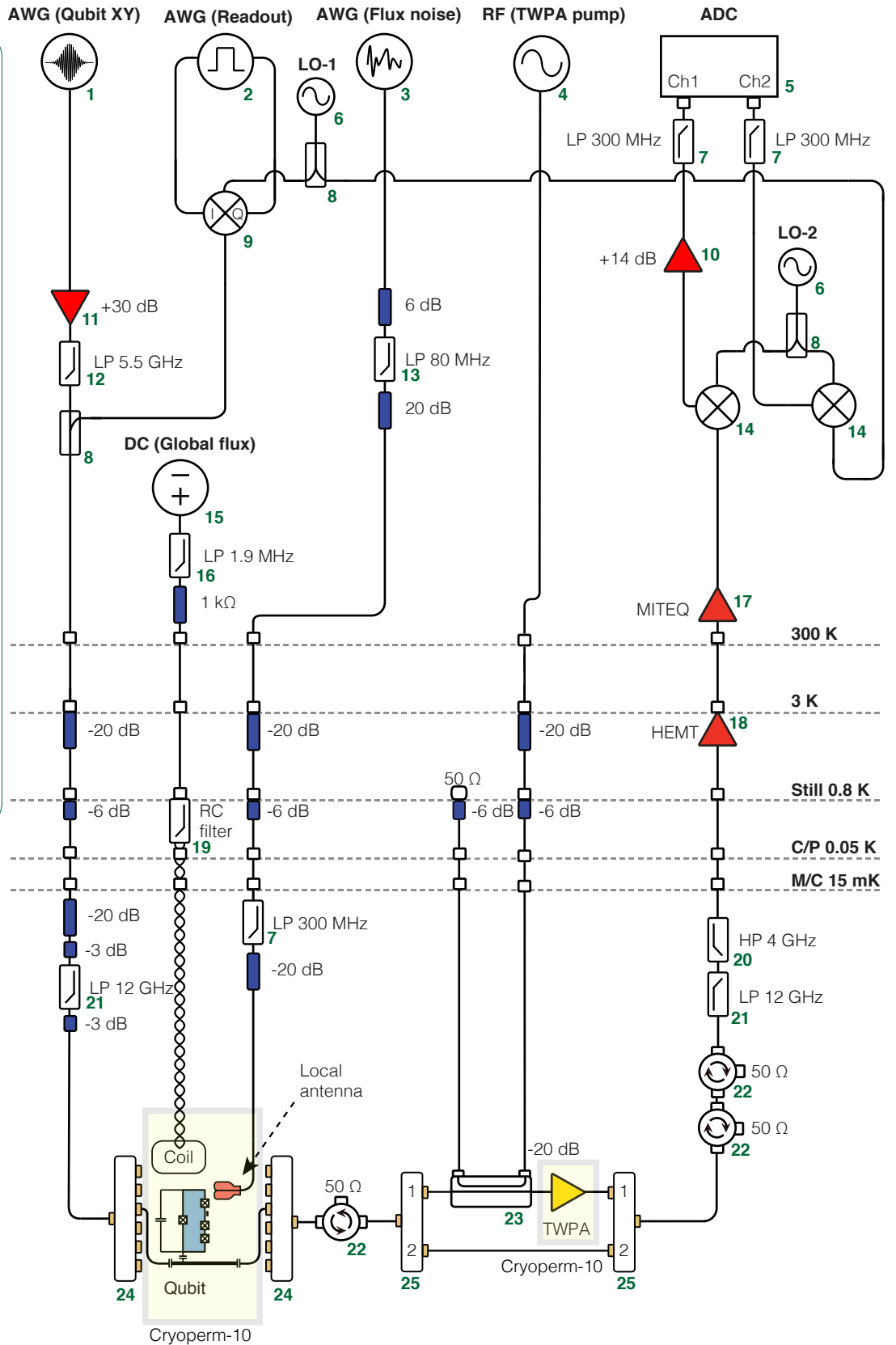


Figure S2. Electronics and control wiring

1.4 Generation of engineered noise

To synthesize a zero-mean flux-noise process $\Delta\Phi(t) \equiv \Phi(t) - \Phi_0/2$ with a given PSD, we use an AWG to produce sample waveforms consisting of N_h harmonics

$$\Delta\Phi(t) = \sum_{m=1}^{N_h} (a_m \cos \omega_m t + b_m \sin \omega_m t), \quad (11)$$

where $\omega_m = 2\pi m/T_0$, and with $2\pi/T_0$ the fundamental angular frequency. The Fourier coefficients a_m and b_m are random variables with

$$\mathbb{E}[a_m] = \mathbb{E}[b_m] = 0, \quad \forall m, \quad \mathbb{E}[a_m b_n] = 0, \quad \forall m, n, \quad \mathbb{E}[a_m a_n] = \mathbb{E}[b_m b_n] = 0, \quad \forall m \neq n. \quad (12)$$

Further taking a_m and b_m to have normal (Gaussian) distributions with variance $\sigma_m^2 = 2S_\Phi(\omega_m)/T_0$, the waveforms $\Delta\Phi(t)$ become a discrete approximation of a Gaussian stochastic process with a frequency-domain PSD $S_\Phi(\omega)$.

In all experiments presented in the main text, we consider

$$S_\Phi(\omega) = \frac{P_0/\pi\omega_c}{1 + (\omega/\omega_c)^2}. \quad (13)$$

with P_0 the noise power and $\omega_c/2\pi = 0.5$ MHz. For the experiment presented in Fig. 2 of the main text, to produce a discrete approximation of a noise process with this spectrum, we take $T_0 = 20$ μ s and $N_h = 10^3$, corresponding to harmonics separated by the fundamental frequency $1/T_0 = 50$ kHz with a high-frequency cutoff at $\omega_{N_h}/2\pi = N_h/T_0 = 50$ MHz. For the experiment presented in Figs. 4 and 5 of the main text, we take $T_0 = 200$ μ s and $N_h = 10^4$, yielding harmonics separated by $1/T_0 = 5$ kHz with the same high-frequency cutoff at $\omega_{N_h}/2\pi = N_h/T_0 = 50$ MHz. A new waveform is produced by the AWG for each measurement of a Pauli operator performed on the qubit to ensure statistical independence of the samples of the stochastic process, leading to a total number of noise samples of 40,000 for the experiment presented in Fig. 2, and 80,000 for Figs 4 and 5. The waveforms have a duration of 1.25 μ s for the experiment presented in Fig. 2 and 20 μ s for Figs. 4 and 5.

1.5 Control pulse sequences

The set of control pulse sequences designed for reconstructing the bispectrum are summarized in Table S2 and visualized in Fig. S3. Note that all control pulse sequences start and end with a $\pi/2$ pulse for the purposes of state preparation and tomography.

Table S2. Control pulse sequences designed for non-Gaussian spectral estimation.

Seq. Index p	Position of π pulses [ns]	Repetitions M	Filter function at zero frequency $F_p(0, T)$
1	No pulses (free evolution)	1	$\neq 0$
2	125, 175, 225, 275, 325, 610, 820, 875	10	$\neq 0$
3	90, 235, 410, 555, 730, 875	10	$\neq 0$
4	80, 150, 205, 355, 560, 630, 685, 835	10	$\neq 0$
5	105, 240, 345, 480, 585, 720, 825, 960	10	$\neq 0$
6	85, 135, 185, 240, 455, 775, 825, 880	10	0
7	130, 180, 285, 335, 475, 765, 870, 960	10	0
8	90, 150, 200, 305, 500, 715, 860, 960	10	0
9	80, 320, 370, 425, 600, 650, 720, 855	10	0
10	205, 310, 360, 545, 645, 725, 850, 960	10	0
11	145, 365, 425, 495, 600, 680, 850, 960	10	0

1.6 Monte Carlo simulations

For the Monte Carlo simulations that are presented in the main text, we consider a single qubit controlled via a microwave drive at angular frequency ω_d , which is used to apply pulses about σ_x and σ_y . In contrast with the main text, here we do not assume that these pulses are instantaneous. To describe the time-evolution of the qubit under the combined action of these finite-width pulses and classical noise described by the process $B(t)$, we consider the Hamiltonian in the lab frame,

$$H(t) = \frac{\omega_q + B(t)}{2} \sigma_z + \varepsilon(t) \cos[\omega_d t + \theta(t)] \sigma_x, \quad (14)$$

where ω_q is the qubit angular frequency, and $\varepsilon(t)$ and $\theta(t)$ are the drive amplitude and phase, respectively.

We next move to the frame that rotates at the drive frequency by applying the unitary transformation $R_d(t) = \exp(-i\omega_d t \sigma_z/2)$, leading to the Hamiltonian $H_d(t) = R_d^\dagger(t)H(t)R_d(t) - iR_d^\dagger(t)\dot{R}_d(t)$ in the rotating frame. This gives

$$H_d(t) = \frac{D + B(t)}{2} \sigma_z + H_c(t), \quad (15)$$

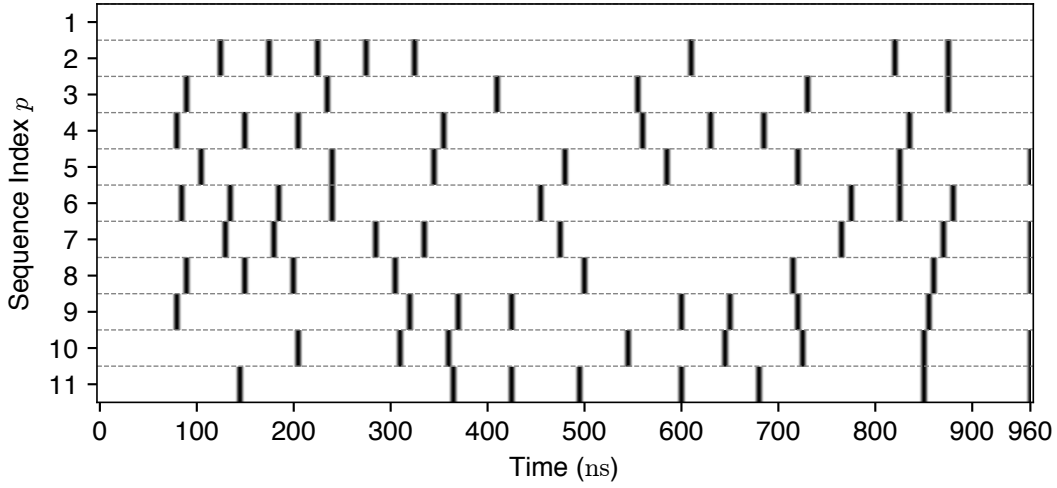


Figure S3. Timing diagrams of the base control sequences. Only π pulses are shown.

where $D \equiv \omega_q - \omega_d$ is the drive detuning and $H_c(t) \equiv \varepsilon(t) \cos[\omega_d t + \theta(t)][\sigma_+ \exp(i\omega_d t) + \text{H.c.}]$ is the control Hamiltonian. Assuming that $\varepsilon(t) \ll \omega_d$ and that $\theta(t)$ varies on a timescale much longer than $2\pi/\omega_d$ allows us to invoke the rotating-wave approximation, under which terms oscillating like $\exp\{\pm[2i\omega_d t + \theta(t)]\}$ are neglected. The resulting control Hamiltonian may be simplified as

$$H_c(t) \approx \frac{1}{2} [\eta_I(t)\sigma_x + \eta_Q(t)\sigma_y], \quad (16)$$

where $\eta_I(t) \equiv \varepsilon(t) \cos \theta(t)$ and $\eta_Q(t) \equiv \varepsilon(t) \sin \theta(t)$ are the envelopes of the in-phase and quadrature components of the microwave control signal, respectively. Equation (16) then describes finite-width pulses about x or y axes.

We perform Monte Carlo simulations by solving the time-dependent Schrödinger equation associated with the Hamiltonian $H_d(t)$ given by Eq. (15), under the control Hamiltonian of Eq. (16). The drive detuning D is set to zero in the simulations. The envelope of each control pulse is cosine with total pulse duration 11 ns (see inset of Fig. S1).

In our Monte Carlo simulations, we account for non-Gaussian noise by setting $B(t) \equiv \beta_\Phi \Delta\Phi(t)^2$ in Eq. (15), and producing random samples of Gaussian flux-noise $\Delta\Phi(t)$ through the approach described in Section 1.4 of this Supplement. Because this approach relies on an exact solution of the qubit evolution under the noise samples, it is equivalent to accounting for all the terms in the cumulant expansion. The fundamental frequency $1/T_0$ and the number of harmonics N_h involved in the Fourier-series representation of the noise process are the same as in Section 1.4. To perform the simulations, we generate 100,000 noise samples for the data presented in Fig. 2 of the main text, and 80,000 noise samples for Figs. 4 and 5.

2 Additional theoretical detail on estimation procedure

2.1 Estimation of the noise mean

2.1.1 Ramsey estimation protocol

To measure the noise mean μ_B , we use the Ramsey sequence illustrated in Fig. S4a. In this sequence, $\pi/2$ pulses about σ_x and σ_y are applied at times $t = 0$ and $t = T$, respectively, followed by a measurement of the qubit in the σ_z eigenbasis at time $t_f = T + \Delta T$, where ΔT is a buffer time much shorter than T , but longer than the pulse width. To lay down the theoretical basis of the procedure, we start from the rotating-frame Hamiltonian $H_d(t)$ introduced in Eq. (15), above. To describe the effects of control with finite-width pulses, it is useful to move to the toggling frame using the unitary transformation $R_T(t) = \mathcal{T} \exp[-i \int_0^t ds H_c(s)]$, with \mathcal{T} the time-ordering operator, and where $H_c(t)$ is given by Eq. (16). In this toggling frame, the Hamiltonian is

$$H_T(t) = \frac{D + B(t)}{2} \vec{y}_p(t) \cdot \vec{\sigma}, \quad \vec{\sigma} \equiv (\sigma_x, \sigma_y, \sigma_z), \quad (17)$$

where $\vec{y}_p(t)$ has components $y_{p,a}(t) \equiv \frac{1}{2} \text{Tr}[R_T^\dagger(t) \sigma_a R_T(t) \sigma_a]$, with $a \in \{x, y, z\}$, for pulse sequence p . Remark that a pulse sequence consisting of instantaneous π pulses (instead of the Ramsey sequence considered here) would result in $\vec{y}_p(t) = [0, 0, y_p(t)]$, where $y_p(t)$ is the switching function used in the main text.

Moving back to the lab frame, the expectation of the z component of the qubit polarization after the pulse sequence is

$$\langle \sigma_z(t_f) \rangle = \mathbb{E} \left\{ \text{Tr} \left[R_T^\dagger(t_f) \sigma_z R_T(t_f) U_T(t_f) \rho_0 U_T^\dagger(t_f) \right] \right\}, \quad (18)$$

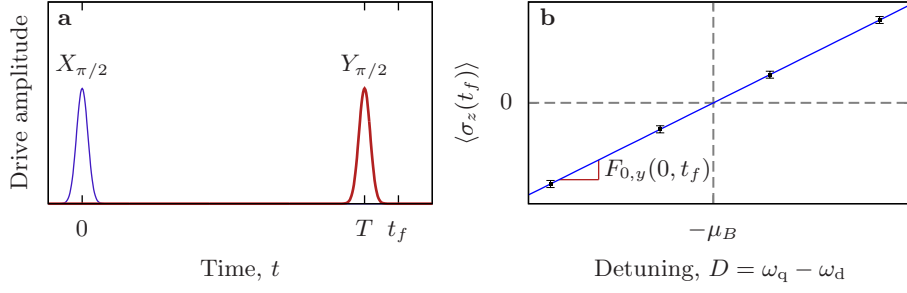


Figure S4. Ramsey protocol for estimation of the noise mean. **a**, Envelopes $\eta_I(t)$ (thin blue line) and $\eta_Q(t)$ (thick red line) of the in-phase and quadrature components of the $\pi/2$ pulses applied about σ_x and σ_y , respectively (see Eq. (16) in the text). **b**, Illustration of the technique for estimation of the mean by linear regression. Black error bars: Monte Carlo simulations of the z component of the qubit polarization $\langle \sigma_z(t_f) \rangle$ after the pulse sequence as a function of the detuning of the drive from the qubit frequency. Blue line: linear regression. According to Eq. (20), the x -intercept of the blue line gives $-\mu_B$, and its slope gives the filter function $F_{0,y}(0, t_f)$, defined below Eq. (19).

where $U_T(t) \equiv \mathcal{T} \exp[-i \int_0^t ds H_T(s)]$ is the time-evolution operator in the toggling frame, and ρ_0 is the initial qubit density matrix, before application of the pulses. We evaluate $\langle \sigma_z(t_f) \rangle$ perturbatively by performing a Dyson expansion of $U_T(t)$. Assuming that t_f is sufficiently short and that $D + B(t)$ is sufficiently small, we truncate this expansion to the first order in $D + B(t)$. Upon substitution into Eq. (18), this approach is equivalent to neglecting any contribution of cumulants of the noise beyond order 1. Taking $\rho_0 \equiv |0\rangle\langle 0|$, with $|0\rangle$ the eigenstate of σ_z with eigenvalue -1 , then yields

$$\langle \sigma_z(t_f) \rangle \approx -y_{p,z}(t_f) + (D + \mu_B) [F_{p,x}(0, t_f)y_{p,y}(t_f) - F_{p,y}(0, t_f)y_{p,x}(t_f)], \quad (19)$$

where we have introduced the filter functions $F_{p,a}(\omega, t) \equiv \int_0^t ds e^{-i\omega s} y_{p,a}(s)$, with $a \in \{x, y, z\}$. For the pulse sequence illustrated in Fig. S4a (which we label by $p = 0$), neglecting any overlap between the pulses, it is straightforward to show that $\vec{y}_p(t_f) \equiv \vec{y}_0(t_f) = (-1, 0, 0)$ for $t_f = T + \Delta t$, leading to

$$\langle \sigma_z(t_f) \rangle \approx (D + \mu_B)T', \quad (20)$$

where $T' \equiv F_{0,y}(0, t_f) = \int_0^{t_f} ds y_{0,y}(s)$ can be viewed as an effective pulse interval accounting for the shape of the pulses. For instantaneous pulses, $T' = T$.

According to Eq. (20), setting $D = 0$, the first noise cumulant $C^{(1)}(0) \equiv \mu_B$ may be estimated simply by measuring $\langle \sigma_z(t_f) \rangle$ and evaluating $\langle \sigma_z(t_f) \rangle / F_{0,y}(0, t_f)$. However, this approach requires accurate knowledge of $F_{0,y}(0, t_f)$, and thus of the shape of the control pulses. For the short Ramsey sequences required here to neglect cumulants of order higher than one in Eqs. (19)-(20), the estimate of μ_B then becomes excessively sensitive to distortions of the pulse envelopes that occur in practice. As a result, estimates of μ_B become significantly biased. Since the bispectrum estimation technique that will be discussed in Sec. 2.3 requires precise knowledge of μ_B , this bias precludes accurate non-Gaussian QNS.

2.1.2 Robust implementation via linear regression

Crucially, the vulnerability of the above Ramsey scheme to pulse-width effects can be alleviated by estimating μ_B with a linear regression procedure. Indeed, according to Eq. (20), plotting $\langle \sigma_z(t_f) \rangle$ as a function of the detuning D results in a straight line that intersects with the abscissa at $D = -\mu_B$ (Fig. S4b), *irrespective of* $F_{0,y}(0, t_f)$. Therefore, measuring $\langle \sigma_z(t_f) \rangle$ as a function of D and performing a linear fit of the resulting data leads to an estimate of μ_B that is insensitive to the pulse shape to the first order in $D + B(t)$.

To apply this idea to our experimental data, we now explicitly construct an estimator of μ_B based on linear regression. For each drive detuning D_j , with $j \in \{1, 2, \dots, N_D\}$, we consider N projective measurements of σ_z yielding outcomes $Z_{j,i} = +1$ or $Z_{j,i} = -1$, where i labels measurements. In the limit $N \gg 1$, the sample mean \bar{Z}_j of the projective measurements for detuning D_j becomes Gaussian distributed,

$$\bar{Z}_j \equiv \frac{1}{N} \sum_{i=1}^N Z_{j,i} \sim \text{Normal} \left[(D_j + \mu_B)F_{0,y}(0, t_f), \frac{\text{var}(\sigma_z)_j}{N} \right], \quad (21)$$

where $\text{var}(\sigma_z)_j \equiv \langle \sigma_z(t_f)^2 \rangle_j - \langle \sigma_z(t_f) \rangle_j^2$ is the expected variance of σ_z averaged over realizations of the noise process, for detuning D_j . Assuming that $\text{var}(\bar{Z}_j) = \text{var}(\sigma_z)_j / N$ is the same for all relevant detunings, $\text{var}(\bar{Z}_j) \equiv \text{var}(\bar{Z}) \forall j$, Eq. (21) then corresponds to the *conditional normal model of linear regression* [S4], in which deviations of the data points from the expected linear behavior are given by independent and identically distributed (i.i.d.) Gaussian random variables. This assumption of uniform variance is justified in an approximate sense for ideal projective measurements. Indeed, in this situation, $\text{var}(\bar{Z}_j) = [1 - \langle \sigma_z(t_f) \rangle_j^2] / N$, so that $\text{var}(\bar{Z}_j)$ is independent of D_j to first order in $\langle \sigma_z(t_f) \rangle_j \approx (D + \mu_B)F_{0,y}(0, t_f)$, with $\text{var}(\bar{Z}_j) \approx 1/N$. Limiting ourselves to detunings for which $\langle \sigma_z(t_f) \rangle_j \lesssim 0.05$ (see Fig. 4a), we find that $\text{var}(\bar{Z}_j)$ (estimated from the sample mean of measurements of σ_z) varies by less than 5% across values of D_j .

To define our estimator of μ_B within the conditional normal model of linear regression, we first introduce the quantities $a \equiv \mu_B F_{0,y}(0, t_f)$ and $b \equiv F_{0,y}(0, t_f)$, corresponding to the y -intercept and slope of the linear equation $\langle \sigma_z(t_f) \rangle_j = (D_j +$

$\mu_B)F_{0,y}(0, t_f) \equiv a + b D_j$, respectively. Maximizing the likelihood of a and b with respect to measurement outcomes \bar{Z}_j with the probability distribution given by Eq. (21) then yields the estimators

$$a^{\text{est}} = N_D^{-1} \sum_{j=1}^{N_D} (\bar{Z}_j - b^{\text{est}} D_j), \quad (22)$$

$$b^{\text{est}} = \frac{\sum_j (D_j - N_D^{-1} \sum_k D_k) (\bar{Z}_j - N_D^{-1} \sum_k \bar{Z}_k)}{\sum_j (D_j - N_D^{-1} \sum_k D_k)^2}. \quad (23)$$

The estimators defined by Eqs. (22) and (23) are Gaussian random variables with $E(a^{\text{est}}) = a$, $E(b^{\text{est}}) = b$, and

$$\begin{aligned} \text{var}(a^{\text{est}}) &= \frac{N_D^{-1} \sum_j D_j^2}{\sum_j (D_j - N_D^{-1} \sum_k D_k)^2} \text{var}(\bar{Z}), & \text{var}(b^{\text{est}}) &= \frac{\text{var}(\bar{Z})}{\sum_j (D_j - N_D^{-1} \sum_k D_k)^2}, \\ \text{cov}(a^{\text{est}}, b^{\text{est}}) &\equiv \mathbb{E}[(a^{\text{est}} - a)(b^{\text{est}} - b)] = -\frac{N_D^{-1} \sum_j D_j}{\sum_j (D_j - N_D^{-1} \sum_k D_k)^2} \text{var}(\bar{Z}). \end{aligned}$$

To estimate μ_B , we use

$$\tilde{\mu}_B^{\text{est}} \equiv a^{\text{est}}/b^{\text{est}}. \quad (24)$$

When $\text{var}(a^{\text{est}})^{1/2}$ and $\text{var}(b^{\text{est}})^{1/2}$ are sufficiently small, we expand $\tilde{\mu}_B^{\text{est}}$ in powers of $\delta a^{\text{est}} \equiv a^{\text{est}} - a$ and $\delta b^{\text{est}} \equiv b^{\text{est}} - b$. Truncating to the first order in δa^{est} and δb^{est} , $\tilde{\mu}_B^{\text{est}}$ becomes approximately Gaussian-distributed with $\mathbb{E}(\tilde{\mu}_B^{\text{est}}) \approx \mu_B$ and

$$\text{var}(\tilde{\mu}_B^{\text{est}}) \approx \frac{b^2 \text{var}(a^{\text{est}}) + a^2 \text{var}(b^{\text{est}}) - 2ab \text{cov}(a^{\text{est}}, b^{\text{est}})}{b^4}. \quad (25)$$

For the experimental data presented in Fig. 4a of the main text, $\text{var}(\tilde{\mu}_B^{\text{est}})$ is estimated by replacing $a \rightarrow a^{\text{est}}$ and $b \rightarrow b^{\text{est}}$ in Eq. (25), with a^{est} and b^{est} given by Eqs. (22) and (23), respectively.

Finally, to isolate the shift in the qubit frequency due to the first cumulant of the engineered source of noise, we apply the above procedure first in the absence of noise, and then in its presence. This yields the two sets of data points shown in Fig. 4a of the main text. Fitting a straight line through each data set and subtracting their x -intercept then gives our final estimate of μ_B , $\mu_B^{\text{est}} = \mu_B^{\text{on}} - \mu_B^{\text{off}}$, where $\mu_B^{\text{on(off)}}$ is the estimator defined by Eq. (24) with (μ_B^{on}) or without (μ_B^{off}) engineered noise. The variance of μ_B^{est} is then simply $\text{var}(\mu_B^{\text{est}}) = \text{var}(\mu_B^{\text{on}}) + \text{var}(\mu_B^{\text{off}})$. For the experimental data presented in the main text, we find $\mu_B^{\text{est}}/2\pi = 127.1$ kHz with a standard deviation $\text{var}(\mu_B^{\text{est}})^{1/2} = 3.86$ kHz, corresponding to the 95% confidence interval $\mu_B^{\text{est}}/2\pi = 127.1 \pm 7.56$ kHz.

2.2 PSD estimation procedure

To estimate the PSD, we build on the frequency-comb approach introduced by Alvarez and Suter in Ref. [13]. As detailed in the main text, treating the FFs as frequency combs generates a system of linear equations, solving which determines the PSD sampled at the harmonic frequencies. Rather than solving this system by matrix inversion as in Ref. [13], we employ a statistically-motivated maximum likelihood estimate (MLE), which takes experimental error into account. The likelihood function we use follows from the asymptotic Gaussian distribution of the measured decay constants, which we describe in Sec. 2.2.1. In Sec. 2.2.2, we determine the likelihood, the conditional probability of obtaining a set of decay data conditioned on the actual value of the PSD. The task of maximizing the likelihood can be cast as a linear problem, allowing clear comparison with Ref. [13].

2.2.1 Distribution of the decay constant

The PSD enters the dynamics of the qubit through the decay constant in Eq. (1), which can be obtained from measurements of the transverse Pauli operators, σ_x and σ_y . Let σ_i^{est} denote the estimated expected value of σ_i for $i \in \{x, y\}$ after the qubit has evolved for a time t under control sequence p . In the limit of a large number of measurements, σ_i^{est} is approximately Gaussian distributed with mean $\mu_i = \mathbb{E}[\langle \sigma_i(t) \rangle]$ and variance $\text{var}[\sigma_i^{\text{est}}]$. In terms of the estimated expected values, the estimated decay constant is

$$\chi_p^{\text{est}}(t) = -\frac{1}{2} \ln(\sigma_x^{\text{est}2} + \sigma_y^{\text{est}2}) = -\frac{1}{2} \ln[(\tilde{\sigma}_x^{\text{est}} + \mu_x)^2 + (\tilde{\sigma}_y^{\text{est}} + \mu_y)^2], \quad (26)$$

where $\tilde{\sigma}_i^{\text{est}} = \sigma_i^{\text{est}} - \mu_i$. Note that σ_i^{est} , μ_i and $\tilde{\sigma}_i^{\text{est}}$ on the right side of this expression depend implicitly on the time t . When $\text{var}[\sigma_x^{\text{est}}], \text{var}[\sigma_y^{\text{est}}] \ll 1$, we can expand this expression about $\tilde{\sigma}_x^{\text{est}}, \tilde{\sigma}_y^{\text{est}} \approx 0$, yielding

$$\chi_p^{\text{est}}(t) \approx -\frac{1}{2} \ln(\mu_x^2 + \mu_y^2) - \left(\frac{\mu_y}{\mu_x^2 + \mu_y^2} \right) \tilde{\sigma}_y^{\text{est}} - \left(\frac{\mu_x}{\mu_x^2 + \mu_y^2} \right) \tilde{\sigma}_x^{\text{est}}.$$

Since it is a linear combination of Gaussian distributed random variables, the decay constant is also Gaussian distributed with mean and variance,

$$\mathbb{E}[\chi_p^{\text{est}}(t)] = -\frac{1}{2}\ln(\mu_x^2 + \mu_y^2) = \frac{1}{2\pi} \int_{-\infty}^{\infty} d\omega |F_p(\omega, t)|^2 S(\omega) + \Theta(t^4) \quad (27)$$

$$\text{var}[\chi_p^{\text{est}}(t)] = \left(\frac{\mu_y}{\mu_x^2 + \mu_y^2}\right)^2 \text{var}[\sigma_y^{\text{est}}] + \left(\frac{\mu_x}{\mu_x^2 + \mu_y^2}\right)^2 \text{var}[\sigma_x^{\text{est}}]. \quad (28)$$

2.2.2 Maximum likelihood estimate

Recall from the main text that after $M \gg 1$ repetitions of a control sequence p with cycle time T , the FF in Eq. (27) is an approximate frequency comb, enabling us to write the decay constant as

$$\mathbb{E}[\chi_p^{\text{est}}(MT)] \approx \frac{M}{T} \sum_{k=-\infty}^{\infty} |F_p(k\omega_h, T)|^2 S(k\omega_h).$$

Using the symmetry $S(\omega) = S(-\omega)$, and the decay of the PSD and FF at high frequencies, we can truncate the sum above to a finite number of harmonic frequencies,

$$\mathbb{E}[\chi_p^{\text{est}}(MT)] \approx \frac{M}{T} \sum_{k=0}^{K-1} \left(\frac{2 - \delta_{k,0}}{2}\right) |F_p(k\omega_h, T)|^2 S(k\omega_h).$$

From the expected value above and the variance in Eq. (28), the conditional probability of measuring $\chi_p^{\text{est}}(MT)$ given the actual values of the PSD, $\vec{S} = [S(0), \dots, S(K\omega_h)]^T$, is

$$P[\chi_p^{\text{est}}(MT) | \vec{S}] = \frac{1}{\sqrt{2\pi \text{var}[\chi_p^{\text{est}}(MT)]}} \exp \left\{ -\frac{\left[\chi_p^{\text{est}}(MT) - \frac{M}{T} \sum_{k=0}^{K-1} \left(\frac{2 - \delta_{k,0}}{2}\right) |F_p(k\omega_h, T)|^2 S(k\omega_h)\right]^2}{2 \text{var}[\chi_p^{\text{est}}(MT)]} \right\}. \quad (29)$$

The estimate of the PSD is based on the likelihood or conditional probability of measuring $\vec{\chi} = [\chi_1^{\text{est}}(MT), \dots, \chi_P^{\text{est}}(MT)]^T$ for a set of control sequences $p = 1, \dots, P$ with $P \geq K$. Since the measurements of the decay constant are uncorrelated, the likelihood follows from Eq. (29),

$$P(\vec{\chi} | \vec{S}) = \prod_{p=1}^P P[\chi_p^{\text{est}}(MT) | \vec{S}] = [(2\pi)^P \det \Sigma]^{-\frac{1}{2}} \exp \left[-\frac{1}{2} (\vec{\chi} - \mathbf{B}\vec{S})^T \Sigma^{-1} (\vec{\chi} - \mathbf{B}\vec{S}) \right], \quad (30)$$

where the $P \times P$ covariance matrix has elements $\Sigma_{p,q} = \text{var}[\chi_p^{\text{est}}(MT)] \delta_{p,q}$ and the $P \times K$ reconstruction matrix \mathbf{B} depends on the FFs evaluated at the harmonic frequencies

$$\mathbf{B}_{p,k} = \frac{M}{T} \left(\frac{2 - \delta_{k,0}}{2}\right) |F_p(k\omega_h, T)|^2.$$

Since the likelihood is Gaussian, the maximum likelihood estimate of the PSD is equivalent to the value of \vec{S} that minimizes the argument of the exponential in Eq. (30),

$$\vec{S}^{\text{MLE}} = \underset{\vec{S}}{\text{argmin}} \frac{1}{2} (\vec{\chi} - \mathbf{B}\vec{S})^T \Sigma^{-1} (\vec{\chi} - \mathbf{B}\vec{S}). \quad (31)$$

The least squares estimate of the PSD originally used in Ref. [13], given by $\vec{S}^{\text{LS}} = \mathbf{B}^{-1}\vec{\chi}$, is recovered when $\Sigma = \mathbf{I}$. This implies that all measurements of the decay constant contribute equally to the estimate. In contrast, the dependence of \vec{S}^{MLE} on the actual variances in Σ ensures that measurements with more uncertainty contribute less to the estimate.

In the experiment, the PSD is reconstructed at the harmonics $k = 0, \dots, 7$ using the $P = 11$ control sequences depicted in Fig. (S3), all with cycle time $T = 960$ ns. This differs from the implementation of Ref. [13], which uses CPMG control sequences of varying cycle times. For each control sequence, the transverse Pauli components are measured to obtain σ_x^{est} , σ_y^{est} and $\chi_p^{\text{est}}(MT)$ from Eq. (26). The variances of $\chi_p^{\text{est}}(MT)$, which comprise Σ , follow from Eq. (28) with μ_x and μ_y replaced by the estimated values σ_x^{est} and σ_y^{est} . In principle, the use of $P = 11$ control sequences would enable us to reconstruct the PSD at $K = 11$ harmonics. For the particular set of control sequences we used, however, the reconstruction matrix \mathbf{B} becomes ill-conditioned for $K > 8$, limiting the number of reconstructable harmonics.

2.3 Bispectrum estimation procedure

While this work is based on the non-Gaussian QNS protocol originally proposed in Ref. [41], the estimation procedure we implemented contains several innovations aimed at generalizing the noise model and improving robustness in the presence of experimental error and numerical instability. First, the zero-mean, non-Gaussian noise model of Ref. [41] is insufficient to describe

the square noise engineered in our qubit sensor, which is inherently nonzero mean. This complicates the estimation procedure, since both the bispectrum and the mean enter the qubit dynamics through the phase in Eq. (2). Estimating the bispectrum requires that we disambiguate the phase contribution of the bispectrum from that of the mean, which we accomplish by first estimating the noise mean and then isolating the dynamical contribution of the bispectrum in the non-Gaussian phase. A second key difference is the “single-shot” nature of the current estimation procedure. In Ref. [41], control sequences with non-zero filter order were first used to estimate the bispectrum at “non-zero harmonics”, i.e., $(k_1\omega_h, k_2\omega_h)$ for which $k_1, k_2 \neq 0$. This estimate was combined with subsequent phase measurements to estimate the bispectrum at “zero harmonics”, i.e. $(k_1\omega_h, k_2\omega_h)$ for which $k_1 = 0$ and/or $k_2 = 0$. In the RMLE estimate of the spectrum presented here, both the zeros and the non-zero harmonics are estimated simultaneously, eliminating any compounding of error that can occur in the two-step procedure. The present work also departs from Ref. [41] significantly in its use of a statistically motivated maximum likelihood estimation procedure. As discussed in the main text, the least-squares estimate of Ref. [41] is susceptible to numerical instability and, additionally, does not take measurement error into account.

In the remainder of this section, we fully detail our bispectrum estimation procedure. We begin by describing the probability distribution of the estimated “non-Gaussian” phase angle (ϕ_p), which enables us to derive the likelihood function for the probability of obtaining a particular set of phase data conditioned on the actual value of the bispectrum (Subsection 2.3.3). From the likelihood, the task of reconstructing the bispectrum can be mapped into an RMLE problem, as shown Subsection 2.3.4. The RMLE approach increases numerical stability, accounts for experimental error and allows us to deploy prior knowledge of the bispectrum in the estimation procedure. Since regularization can introduce error into the estimate if it is too strong, in Subsection 2.3.5 we determine an appropriate regularization strength for our problem using the L-curve criterion.

2.3.1 Distribution of the non-Gaussian phase

The non-Gaussian phase of the qubit is determined from the estimated expected values of the transverse Pauli operators, σ_x^{est} and σ_y^{est} , when the qubit has evolved under control sequence p for a time t . Recall from Sec. 2.2 that in the limit of a large number of measurements, σ_i^{est} is approximately Gaussian distributed with mean $\mu_i = \mathbb{E}[\langle\sigma_i(t)\rangle]$ and variance $\text{var}[\sigma_i^{\text{est}}]$. From the estimated expected values, the ordinary phase is determined by

$$\phi_p^{\text{est}}(t) = -\tan^{-1}\left(\frac{\sigma_x^{\text{est}}}{\sigma_y^{\text{est}}}\right) = -\tan^{-1}\left(\frac{\tilde{\sigma}_x^{\text{est}} + \mu_x}{\tilde{\sigma}_y^{\text{est}} + \mu_y}\right), \quad (32)$$

where σ_i^{est} , μ_i and $\tilde{\sigma}_i^{\text{est}} = \sigma_i^{\text{est}} - \mu_i$ depend implicitly on the time t . When $\text{var}[\sigma_x^{\text{est}}], \text{var}[\sigma_y^{\text{est}}] \ll 1$, we can expand ϕ_p^{est} about $\tilde{\sigma}_x^{\text{est}}$, $\tilde{\sigma}_y^{\text{est}} \approx 0$, yielding

$$\phi_p^{\text{est}}(t) \approx -\tan^{-1}\left(\frac{\mu_x}{\mu_y}\right) - \left(\frac{\mu_y}{\mu_x^2 + \mu_y^2}\right)\tilde{\sigma}_x^{\text{est}} + \left(\frac{\mu_x}{\mu_x^2 + \mu_y^2}\right)\tilde{\sigma}_y^{\text{est}}.$$

As a linear combination of Gaussian distributed random variables, the phase is also Gaussian distributed with mean and variance

$$\begin{aligned} \mathbb{E}[\phi_p^{\text{est}}(t)] &= -\tan^{-1}\left(\frac{\mu_x}{\mu_y}\right) = F_p(0, t)\mu_B - \frac{1}{3!(2\pi)^2} \int_{\mathbb{R}^2} d\vec{\omega} G_p(\vec{\omega}, t) S_2(\vec{\omega}) + \Theta[t^5], \\ \text{var}[\phi_p^{\text{est}}(t)] &= \left(\frac{\mu_y}{\mu_x^2 + \mu_y^2}\right)^2 \text{var}[\sigma_x^{\text{est}}] + \left(\frac{\mu_x}{\mu_x^2 + \mu_y^2}\right)^2 \text{var}[\sigma_y^{\text{est}}]. \end{aligned} \quad (33)$$

The second equality on the right-hand side of $\mathbb{E}[\phi_p^{\text{est}}]$ follows from Eq. (2). Subtracting out the contribution of the noise mean from the phase produces the non-Gaussian phase,

$$\varphi_p^{\text{est}}(t) = \phi_p^{\text{est}}(t) - F_p(0, t)\mu_B^{\text{est}}, \quad (34)$$

where μ_B^{est} is the estimated noise mean described in Sec. 2.1. Using the asymptotic Gaussian distribution of μ_B^{est} with mean μ_B and variance $\text{var}[\mu_B^{\text{est}}]$, the non-Gaussian phase is similarly Gaussian with mean and variance

$$\mathbb{E}[\varphi_p^{\text{est}}(t)] = -\frac{1}{3!(2\pi)^2} \int_{\mathbb{R}^2} d\vec{\omega} G_p(\vec{\omega}, t) S_2(\vec{\omega}) + \Theta[t^5], \quad (35)$$

$$\text{var}[\varphi_p^{\text{est}}(t)] = \left(\frac{\mu_y}{\mu_x^2 + \mu_y^2}\right)^2 \text{var}[\sigma_x^{\text{est}}] + \left(\frac{\mu_x}{\mu_x^2 + \mu_y^2}\right)^2 \text{var}[\sigma_y^{\text{est}}] + F_p(0, t)^2 \text{var}[\mu_B^{\text{est}}]. \quad (36)$$

Note that $\mathbb{E}[\varphi_p^{\text{est}}(t)]$ depends to leading order on the bispectrum, unlike $\mathbb{E}[\phi_p^{\text{est}}(t)]$ above.

2.3.2 Restriction to the principal domain

For any real, classical process, the bispectrum has three general symmetries: (1) $S_2(\omega_1, \omega_2) = S_2(\omega_2, \omega_1)$ (permutation symmetry); (2) $S_2(\omega_1, \omega_2) = S_2(-\omega_1, -\omega_2)$ (invariance under complex conjugation); (3) $S_2(\omega_1, \omega_2) = S_2(-\omega_1 - \omega_2, \omega_2)$ (stationarity). These symmetries define the 12 regions of the frequency plane depicted in Fig. 3c. If $(\omega_1, \omega_2) \in \text{int}(\mathcal{D}_2)$ is contained in the interior of the principal domain, the symmetries imply

$$\begin{aligned} S_2(\omega_1, \omega_2) &= S_2(\omega_2, \omega_1) = S_2(-\omega_2, \omega_1 + \omega_2) = S_2(-\omega_1, \omega_1 + \omega_2) = S_2(-\omega_1 - \omega_2, \omega_1) = S_2(-\omega_1 - \omega_2, \omega_2) = \\ &= S_2(-\omega_1, -\omega_2) = S_2(-\omega_2, -\omega_1) = S_2(\omega_2, -\omega_1 - \omega_2) = S_2(\omega_1, -\omega_1 - \omega_2) = S_2(\omega_1 + \omega_2, -\omega_1) = S_2(\omega_1 + \omega_2, -\omega_2). \end{aligned}$$

In other words, the bispectrum takes a value equivalent to $S_2(\omega_1, \omega_2)$ in each of the 12 regions. This is summarized by the multiplicity, $m(\omega_1, \omega_2) = 12$. For (ω, ω) , which lies on the boundary of \mathcal{D}_2 ,

$$S_2(\omega, \omega) = S_2(-\omega, -\omega) = S_2(-2\omega, \omega) = S_2(\omega, -2\omega) = S_2(2\omega, -\omega) = S_2(-\omega, 2\omega),$$

implying $m(\omega, \omega) = 6$. For $(\omega, 0)$, which also lies on the boundary of \mathcal{D}_2 ,

$$S_2(\omega, 0) = S_2(0, \omega) = S_2(-\omega, 0) = S_2(0, -\omega) = S_2(\omega, -\omega) = S_2(\omega, -\omega),$$

similarly implying $m(\omega, 0) = 6$. Note that $(\omega_1, \omega_2) = (0, 0)$ is invariant under all of the symmetries, implying that $m(0, 0) = 1$.

The symmetries and multiplicities simplify the expected value of the phase substantially. Recall that after $M \gg 1$ repetitions of control sequence p with cycle time T , the frequency comb approximation enables us to write the expected phase as a discrete sum depending on the bispectrum and the FF evaluated at the harmonic frequencies,

$$\mathbb{E}[\varphi_p^{\text{est}}(MT)] = -\frac{1}{3!(2\pi)^2} \int_{\mathbb{R}^2} d\vec{\omega} G_p(\vec{\omega}, MT) S_2(\vec{\omega}) \approx -\frac{M}{3!T^2} \sum_{\vec{k} \in \mathbb{Z}^2} G_p(\omega_h \vec{k}, T) S_2(\omega_h \vec{k}).$$

In terms of the multiplicities, we can rewrite the sum as

$$\begin{aligned} \mathbb{E}[\varphi_p^{\text{est}}(MT)] &\approx -\frac{12M}{3!T^2} \sum_{\omega_h \vec{k} \in \text{int}(\mathcal{D}_2)} G_p(\omega_h \vec{k}, T) S_2(\omega_h \vec{k}) - \frac{6M}{3!T^2} \sum_{k \in \mathbb{Z}} G_p(\omega_h k, \omega_h k, T) S_2(\omega_h k, \omega_h k) \\ &\quad - \frac{6M}{3!T^2} \sum_{k \in \mathbb{Z}} G_p(\omega_h k, 0, T) S_2(\omega_h k, 0) - \frac{M}{3!T^2} G_p(0, 0, T) S_2(0, 0) \\ &= -\frac{M}{3!T^2} \sum_{\omega_h \vec{k} \in \mathcal{D}_2} m(\omega_h \vec{k}) G_p(\omega_h \vec{k}, T) S_2(\omega_h \vec{k}). \end{aligned}$$

Using $S_2(\omega_h \vec{k}) = S_2(-\omega_h \vec{k})$ and $G_p(\omega_h \vec{k}, T)^* = G_p(-\omega_h \vec{k}, T)$, and truncating the sum to a finite subset \mathcal{K}_2 , we obtain

$$\mathbb{E}[\varphi_p^{\text{est}}(MT)] \approx -\frac{M}{3!T^2} \sum_{\vec{k} \in \mathcal{K}_2} m(\omega_h \vec{k}) \text{Re}[G_p(\omega_h \vec{k}, T)] S_2(\omega_h \vec{k}). \quad (37)$$

2.3.3 Likelihood function $P(\vec{\varphi} | \vec{S}_2)$

Given the actual bispectrum in \mathcal{K} , $\vec{S}_2 = [S_2(\omega_h \vec{k}_1), \dots, S_2(\omega_h \vec{k}_N)]^T$, the conditional probability of measuring $\varphi_p^{\text{est}}(MT)$ follows from Eqs. (35)-(37),

$$P[\varphi_p^{\text{est}}(MT) | \vec{S}_2] = \frac{1}{\sqrt{2\pi \text{var}[\varphi_p^{\text{est}}(MT)]}} \exp \left\{ -\frac{\left[\varphi_p^{\text{est}}(MT) + \frac{M}{3!T^2} \sum_{\vec{k} \in \mathcal{K}} m(\omega_h \vec{k}) \text{Re}[G_p(\omega_h \vec{k}, T)] S_2(\omega_h \vec{k}) \right]^2}{2 \text{var}[\varphi_p^{\text{est}}(MT)]} \right\}. \quad (38)$$

Reconstructing the bispectrum requires measurements the non-Gaussian phase for a set of control sequences $p = 1, \dots, P$ with $P \geq N$, which we gather into the column vector $\vec{\varphi} = [\varphi_1^{\text{est}}(MT), \dots, \varphi_P^{\text{est}}(MT)]^T$. Because the non-Gaussian phase measurements are uncorrelated, the likelihood or probability of obtaining $\vec{\varphi}$ given \vec{S}_2 is a product of the conditional probabilities for the complete set of control sequences,

$$P(\vec{\varphi} | \vec{S}_2) = \prod_{p=1}^P P[\varphi_p^{\text{est}}(MT) | \vec{S}_2] = [(2\pi)^P \det \mathbf{\Sigma}]^{-\frac{1}{2}} \exp \left[-\frac{1}{2} (\vec{\varphi} - \mathbf{A} \vec{S}_2)^T \mathbf{\Sigma}^{-1} (\vec{\varphi} - \mathbf{A} \vec{S}_2) \right]. \quad (39)$$

Here, the $P \times P$ covariance matrix $\mathbf{\Sigma}$ is diagonal with elements $\Sigma_{p,q} = \text{var}[\varphi_p^{\text{est}}(MT)] \delta_{p,q}$, and the $P \times N$ reconstruction matrix \mathbf{A} depends on the filter functions evaluated at the harmonic frequencies,

$$(\mathbf{A})_{p,n} = -\frac{M}{3!T^2} m(\omega_h \vec{k}_n) \text{Re}[G_p(\omega_h \vec{k}_n, T)]. \quad (40)$$

In the experiment, the likelihood in Eq. (39) is determined by measuring the non-Gaussian phase for each of the $P = 11$ control sequences in Fig. (S3). Since we also rely on these sequences to estimate the PSD, both the bispectrum and the PSD can be estimated with the the same set of transverse Pauli measurements. For each of the control sequences, $\varphi_p^{\text{est}}(MT)$ was determined from Eq. (32) using measurements of σ_x^{est} , σ_y^{est} and μ_B^{est} . The variances of the $\varphi_p^{\text{est}}(MT)$, which constitute the covariance matrix $\mathbf{\Sigma}$, are given by Eq. (36) with μ_x and μ_y replaced by the estimated values σ_x^{est} , σ_y^{est} . The reconstruction matrix \mathbf{A} is determined from Eq. (40), with each FF evaluated on the set of harmonics \mathcal{K}_1 depicted in Fig. 3(b).

2.3.4 Regularized maximum likelihood estimation

For the Gaussian likelihood derived in the previous section, the maximum likelihood estimate (MLE) of the bispectrum is equivalent to the value of \vec{S}_2 that minimizes the exponent in Eq. (39),

$$\vec{S}_2^{\text{MLE}} = \underset{\vec{S}_2}{\operatorname{argmin}} \frac{1}{2} (\vec{\varphi} - \mathbf{A}\vec{S}_2)^T \Sigma^{-1} (\vec{\varphi} - \mathbf{A}\vec{S}_2). \quad (41)$$

In the special case where $\Sigma \propto \mathbf{I}$, we recover the least-squares estimate used in Ref. [41] with solution $\vec{S}_2^{\text{LS}} = \mathbf{A}^{-1}\vec{\varphi}$. Even with a nonuniform covariance matrix, Eq. (41) is a simple convex optimization problem admitting an analytic solution for \vec{S}_2^{MLE} . When \mathbf{A} is ill-conditioned, however, the MLE suffers from numerical instability, which can introduce significant error into the estimate of the bispectrum, despite the existence of an analytic solution. The problem can be made more stable by introducing a regularization term or “regularizer” $Q(\vec{S}_2)$, producing the regularized maximum likelihood estimate (RMLE) of the bispectrum,

$$\vec{S}_2^{\text{RMLE}} = \underset{\vec{S}_2}{\operatorname{argmin}} \left[\frac{1}{2} (\mathbf{A}\vec{S}_2 - \vec{\varphi})^T \Sigma^{-1} (\mathbf{A}\vec{S}_2 - \vec{\varphi}) + Q(\vec{S}_2) \right]. \quad (42)$$

The regularizer imposes additional structure on the solution, making it more robust to numerical instability arising from \mathbf{A} . It also prevents overfitting, in which the estimated bispectrum is unduly influenced by errors in $\vec{\varphi}$ and is, thus, a poor predictor of the qubit dynamics under more general control settings.

There are numerous methods of regularization for ill-conditioned and/or ill-posed problems. An approach particularly amenable to maximum likelihood estimation is Tikhonov regularization, which employs an L2 regularizer $Q(\vec{S}_2) = \|\lambda\vec{S}_2\|_2^2$ with strength controlled by the regularization parameter $\lambda \geq 0$ [S5]. In Eq. (42), this regularizer has the effect of penalizing \vec{S}_2 with larger L_2 -norms. To estimate the bispectrum, we consider a variation of Tikhonov regularization in which

$$Q(\vec{S}_2) = \|\lambda \mathbf{D} \vec{S}_2\|_2^2, \quad (43)$$

where $\mathbf{D} = \operatorname{diag}(d_1, \dots, d_N)$ is the diagonal “smoothing matrix”. Note that the Tikhonov regularizer is recovered when $d_1 = \dots = d_N = 1$ (Fig. S5a) and the standard maximum likelihood estimate is recovered when $\lambda = 0$. Using non-uniform values for the diagonals enables us to incorporate prior information about the bispectrum. For example, if the magnitude of the bispectrum is known to decay at the high-frequency border of \mathcal{K} , we can make the corresponding harmonics in \mathbf{D} large compared to those of the interior (Fig. S5b). Such a smoothing matrix favors a solution with small magnitude at the border. The connection between the smoothing matrix and prior knowledge of the bispectrum is more explicit in a Bayesian formulation of the estimation problem in which the RMLE estimate in Eq. (42) with the regularizer in Eq. (43) is equivalent to a posterior mean estimate in which the prior distribution of the bispectrum is Gaussian and zero-mean with covariance matrix $(2\lambda^2 \mathbf{D}^2)^{-1}$, provided \mathbf{D} is full-rank. For any smoothing matrix, the regularized maximum likelihood estimate has the simple analytic solution,

$$\vec{S}_2^{\text{RMLE}} = (\mathbf{A}^T \Sigma^{-1} \mathbf{A} + 2\lambda^2 \mathbf{D}^2)^{-1} (\mathbf{A}^T \Sigma^{-1} \vec{\varphi}). \quad (44)$$

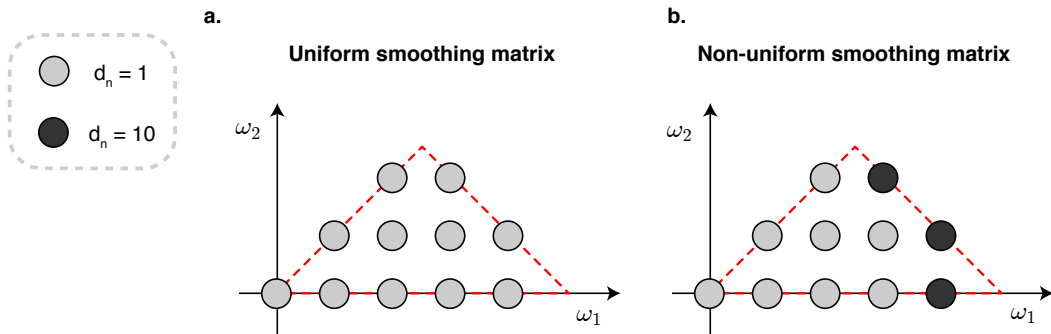


Figure S5. Smoothing matrix \mathbf{D} given a prior information. **a**, A smoothing matrix that assumes the least prior information about the bispectrum. **b**, A smoothing matrix that assumes the bispectrum decays to zero at the border of an octant.

2.3.5 The L-curve criterion

Although it guards against numerical instability and overfitting to errors in the measured data, the regularizer can introduce its own error into the estimate if λ too large. A fundamental challenge in regularization is selecting a value of λ that balances these sources of error. While this problem is still an active area of research, one of the most widely used strategies for selecting λ is the L-curve criterion [S6]. A graphical technique, the L-curve criterion enables one to visualize the magnitude of the regularization error in proportion to other errors in the estimate and choose λ accordingly.

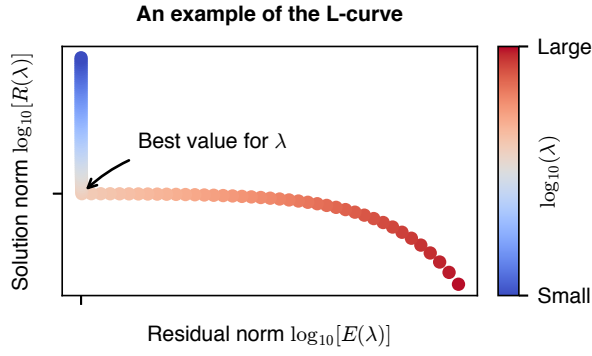


Figure S6. An example of the L-curve plot.

For a given λ , the sources of error that contribute to the regularized maximum likelihood estimate in Eq. (44) are described by the residual norm

$$E(\lambda) \equiv \left[\frac{1}{2} (\mathbf{A} \vec{S}_2^{\text{RMLE}} - \vec{\varphi})^T \boldsymbol{\Sigma}^{-1} (\mathbf{A} \vec{S}_2^{\text{RMLE}} - \vec{\varphi}) \right]^{1/2}. \quad (45)$$

and the solution norm

$$R(\lambda) \equiv \left\| \mathbf{D} \vec{S}_2^{\text{RMLE}} \right\|_2 = \left\| \text{diag}(d_1, \dots, d_{|\mathcal{R}|}) \vec{S}_2^{\text{RMLE}} \right\|_2. \quad (46)$$

The regularization parameter λ enters both the residual norm and solution norm implicitly through \vec{S}_2^{RMLE} . The residual norm increases as λ grows, while the solution norm decreases. When $E(\lambda)$ is too large relative to $R(\lambda)$, the estimate does not account for the measured data due to error introduced by the regularization. Conversely, when $E(\lambda)$ is too small relative to $R(\lambda)$, the estimate fits the measured data too closely, making it susceptible to overfitting and numerical error. The influence of λ on the error contributions is captured by the L-curve, a parametric plot of $\log R(\lambda)$ vs. $\log E(\lambda)$ as a function of λ . A typical L-curve, with its characteristic ‘‘L’’ shape, is shown in Fig. S6. Note that as λ increases from left to right, $\log R(\lambda)$ sharply decreases and then plateaus, while $\log E(\lambda)$ is initially stable followed by a rapid increase. The corner of the L-curve, marks a point at which the solution norm and residual norm are small simultaneously. The corner, thus, signifies the optimal value of λ according to the L-curve criterion.

Figure S7 shows L-curves generated by our experimental data for the two different smoothing matrices illustrated in Fig. S5. For both the uniform and non-uniform smoothing matrices, the L-curves lack corners. Unlike the typical L-curve in Fig. S6, $\log R(\lambda)$ does not exhibit a sharp increase as $\lambda \rightarrow 0$. This indicates that, for the control sequences we have selected, the reconstruction matrix \mathbf{A} is sufficiently well conditioned to make regularization the dominant source of error [S7]. Consequently, it is not optimal to utilize regularization in this setting and the reconstruction presented in the main text uses $\lambda = 0$.

Note that this finding is contingent on both \mathbf{A} and the particular regularizer we employ. Estimating the bispectrum at a greater number of harmonics demands a larger \mathbf{A} , which is more likely to be near singular and/or poorly conditioned. This scenario will likely require some form of regularization. Additionally, the error introduced by regularization is reduced when prior knowledge of the bispectrum (if available) is used to select the regularizer. For example, suppose a noise model or previous experiment indicates that \vec{S}_2 takes a value in the vicinity of \vec{S}_μ . This information is captured by the regularizer

$$Q(\vec{S}_2) = \frac{1}{2} (\vec{S}_2 - \vec{S}_\mu)^T (2\lambda^2 \mathbf{D}^2) (\vec{S}_2 - \vec{S}_\mu). \quad (47)$$

This corresponds to a Gaussian prior distribution of \vec{S}_2 with mean \vec{S}_μ and covariance matrix $(2\lambda^2 \mathbf{D}^2)^{-1}$. In contrast, naively employing Tikhonov regularization amounts to assuming a zero-mean prior distribution of \vec{S}_2 .

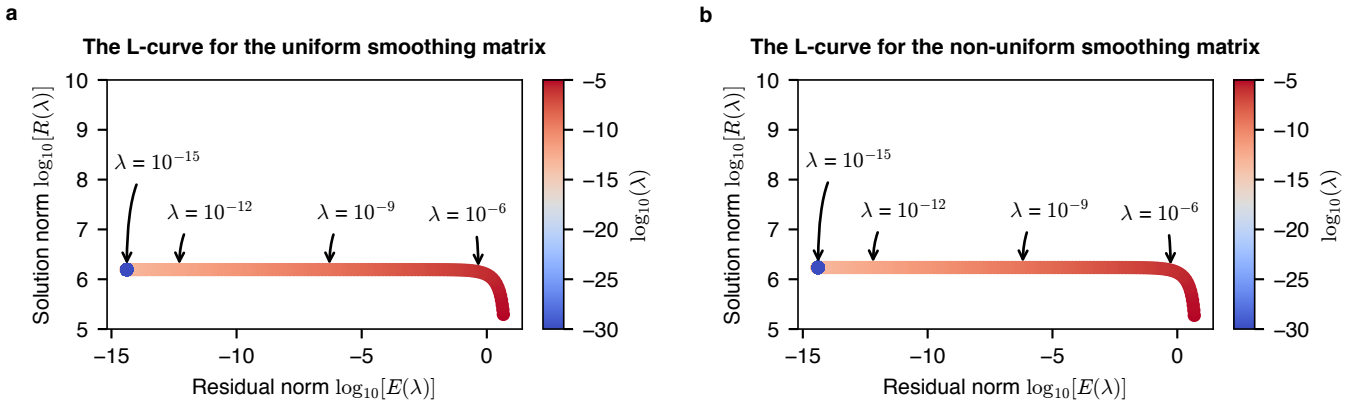


Figure S7. The L-curve plots for experimental data. a, The L-curve plot for the uniform smoothing matrix. **b,** The L-curve plot for the non-uniform smoothing matrix.

Additional references

- S1. V. E. Manucharyan, J. Koch, L. I. Glazman, and M. H. Devoret, “Fluxonium: Single Cooper-pair circuit free of charge offsets,” *Science* **326**, 113–116 (2009).
- S2. E. Magesan, J. M. Gambetta, and J. Emerson, “Scalable and robust randomized benchmarking of quantum processes,” *Phys. Rev. Lett.* **106**, 180504 (2011).
- S3. C. Macklin, K. O’Brien, D. Hover, M. E. Schwartz, V. Bolkhovskiy, X. Zhang, W. D. Oliver, and I. Siddiqi, “A near-quantum-limited Josephson traveling-wave parametric amplifier,” *Science* **350**, 307–310 (2015).
- S4. G. Casella and R. L. Berger, *Statistical Inference* (Duxbury Pacific Grove, CA, 2002).
- S5. A. Tikhonov, “Solution of incorrectly formulated problems and the regularization method,” *Dokl. Akad. Nauk* **151**, 1035–1038 (1963).
- S6. P. C. Hansen, “The L-curve and its use in the numerical treatment of inverse problems,” in *Computational Inverse Problems in Electrocardiology* (WIT Press, 2000) pp. 119–142.
- S7. T. Regińska, “A regularization parameter in discrete ill- posed problems,” *SIAM J. Sci. Comput.* **17**, 740–749 (1996).